# Understanding 2D van der Waals Antiferromagnets: $MnPS_3$ and CrSBr

A Thesis

submitted to

Indian Institute of Science Education and Research Pune in partial fulfilment of the requirements for the BS-MS Dual Degree Programme
By

**Subhrajit Dalai**


Indian Institute of Science Education and Research Pune Dr. Homi Bhabha Road, Pashan, Pune 411008, INDIA

March 2024

Supervisor: **Dr. Aparna Deshpande**

# Certificate

This is to certify that this dissertation entitled '**Understanding 2D van der Waals Antiferromagnets: $MnPS_3$ and CrSBr**' towards the partial fulfillment of the BS-MS dual degree programme at the Indian Institute of Science Education and Research, Pune represents study/work carried out by 'Subhrajit Dalai at Indian Institute of Science Education and Research, Pune' under the supervision of 'Dr. Aparna Deshpande, Assistant Professor, Department of Physics', during the academic year 2023-2024.

**Dr. Aparna Deshpande**

Committee:

Dr. Aparna Deshpande

Dr. Atikur Rahman

**This thesis is dedicated to my family.**

# Declaration

I hereby declare that the matter embodied in the report entitled '**Understanding 2D van der Waals Antiferromagnets: $MnPS_3$ and CrSBr**' are the results of the work carried out by me at the Department of Physics, Indian Institute of Science Education and Research, Pune, under the supervision of Dr. Aparna Deshpande and the same has not been submitted elsewhere for any other degree.

Subhrajit Dalai

**Subhrajit Dalai**

# Acknowledgements

I am very much grateful to my supervisor, Dr. Aparna Deshpande for giving me opportunity to work in STM and Atom manipulation lab under her supervision. Her guidance and support kept me motivate to give my best and work on my project diligently. Due to her support, I am still remained motivate to pursue my PhD in field of condensed matter.

I would like thank my thesis expert member, Dr. Atikur Rahman, for agreeing and guide my thesis. His valuable suggestion and advice helped me in my project.

I would like thank Dr. Sadhu Kolekar (our collaborator) who provided me great opportunity to explore a new material in field of condensed matter. His ideas and guidance also helped me lot in my project.

I would also like thank Dr Ashish Arora, and his student Sourabh Jain, Bhumika for lending and helping in my research project regarding optical measuremnts.

I want to thank my seniors Imran bhaiya, Giriraj bhaiya, Umashankar bhaiya and Vaibhav bhaiya who were like a second supervisor to me and my labmates Piyush Parakh , Pranjal Panwar and Nikhil Singh , for helping me carry out this work. I would like thank Rohan Thangaraj who provided me with transport patterns for my sample.

I want to thank all the technical staff, Nilesh sir, Anil sir, Sudhir sir, and Kartikeyan bhaiya, for providing technical support for running the lab smoothly and data collection.

I would also thank my friends Vinayak, Shivansh, Chayanka, Pratham, Deep and many others who supported me in my 5 years journey of BS-MS. I want to thank my family members, my father and mother, who provided me with emotional and financial support and helped me in fulfilling my long-cherished dream of becoming a physicist. I am very grateful to my elder sisters, who took the responsibility of the family on his shoulders that gave me the freedom to pursue research, and a new family member, my brother-in-law, who joined the family during this work that made the family even more cheerful.

# Abbreviation

| | |
|---|---|
| AFM | Atomic force microscopy |
| vdW | van der Waals |
| QHE | Quantum Hall Effect |
| HR-TEM | High resolution Transmission Electron Microscope |
| LDOS | Local density of states |
| LT-UHV-STM | Low Temperature Ultra-High-Vacuum STM |
| STM | Scanning Tunneling Spectroscopy |
| TSP | Titanium Sublimation Pump |
| FFT | Fast Fourier Transform |
| FM | Ferromagnetism |
| AF | Anti-ferromagnetism |

# Abstract

Low dimensional material shows unique properties as compared to their 3D counterpart, making them extremely fascinating to study. Since 2004 when graphene was first exfoliated by Andre Geim and Konstantin Novoselov, the field of 2d van der Waals material bloomed. 2d van der Waals material contains wide range material such as metals, insulators, semiconductors, superconductors and topological materials. After 2016, researchers' interest in 2D magnets increased as they can used as multifunctional material with wide range of phenomena and promising candidate for next generation information technology. The recent discovery of 2D magnetic ordering in $CrI_3$, $Cr_2Ge_2Te_6$, $VSe_2$ and $Fe_3GeTe_2$ has stimulated to expand the scope of 2D magnets.

In this thesis we will discuss two such material which are antiferromagnetic in nature. $MnPS_3$ is antiferromagnetic semiconductor with wide band gap of 2.64 eV and Neel temperature 78 K. CrSBr is an antiferromagnetic semiconductor with band gap of 1.5 eV and Neel temperature 132 K.

In the first part of the thesis, both $MnPS_3$ and CrSBr were characterized using an Optical microscope, atomic force microscopy, and Raman Spectroscopy. Raman mode found for $MnPS_3$: 275 $cm^{-1}$ and 383 $cm^{-1}$ and CrSBr: 114 $cm^{-1}$, 244 $cm^{-1}$, 344 $cm^{-1}$showing comparing vibrational modes in two different samples. HR-TEM and elemental mapping of CrSBr shows Cr and S have a lower atomic concentration than that of bromine. In second part , Low-temperature STM measurements were performed on a CrSBr single crystal at 77K in the antiferromagnetic phase to understand its electronic correlation. Then, an investigation of intrinsic defects was performed and tried to understand the role played in electron doping. A general trend of valence band upward shift was observed in those defect regions giving a clear indication of an increase in charge carrier density. $MnPS_3$ thin flakes color on $SiO_2$/Si was quantified showing quasi-periodic oscillatory behavior. The optical absorbance spectra were taken at room temperature for thin flakes to understand the light-matter interaction. An optical band gap of 2.7eV was observed in all the flakes.

**Keywords**: 2D magnetism, Anti-ferromagnetic

# Content

# List of Figures

# List Of Tables

# Chapter 1 Introduction

## 1.1 Background

Throughout human history, our innate curiosity has driven us to explore the mysteries of the universe and understand its inner workings. From the primal instincts of early humans to the sophisticated inquiries of modern civilization, there has been an enduring fascination with unraveling the fundamental principles that govern our reality. This pursuit of knowledge has given rise to the discipline of science, a systematic endeavor to observe, record, and explain natural phenomena through experimentation and theoretical frameworks. At the heart of scientific inquiry lies physics, the branch of science concerned with the nature and properties of matter, energy, space-time, and the fundamental forces that shape the universe.

Since antiquity, humans have sought to harness the properties of materials for practical purposes, leading to the categorization of historical epochs based on dominant material usage, such as the Stone Age, Bronze Age, and Iron Age. In the modern era, characterized by the proliferation of information technology, our daily lives are permeated by gadgets and devices that rely on the electronic, magnetic, and optical properties of matter. This intersection of physics and materials science has given rise to the field of condensed matter physics, a cornerstone of modern scientific research.

Condensed matter physics encompasses the study of phenomena arising from the collective behavior of particles in condensed phases, such as solids and liquids. From the enigmatic quantum Hall effect to the marvel of superconductivity and the intricacies of ferromagnetism, condensed matter physics elucidates a diverse array of emergent and exotic phenomena. Theoretical insights and experimental breakthroughs in this field have revolutionized our understanding of complex systems and paved the way for the development of groundbreaking technologies, from smartphones to quantum computers.

At the forefront of condensed matter physics research lies a focus on nanoscale phenomena, cryogenic temperatures, and ultra-high vacuum environments. By probing the behavior of matter at these extremes, scientists push the boundaries of our understanding and unlock new possibilities for technological innovation. From manipulating individual atoms to engineering materials with tailored properties, the exploration of condensed matter physics at the nanoscale holds promise for transformative advancements in fields ranging from electronics to medicine.

In summary, condensed matter physics stands as a testament to humanity's relentless quest for knowledge and innovation. By delving into the intricacies of matter and its interactions, researchers continue to unravel the mysteries of the universe and chart new frontiers in science and technology.

## 1.2 2D materials

### 1.2.1 From 3D to the 2D world

We perceive physical objects in our daily lives as three-dimensional because all matter has a fixed volume that can be specified using three different coordinate systems. In addition, we also see 2D objects as still images from movies or pictures.

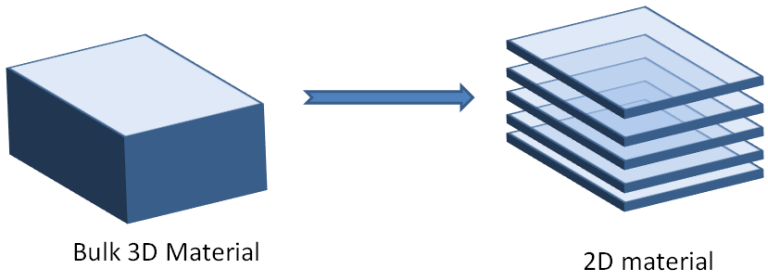


Figure 1.1 : Schematic diagram of 3D bulk material and Quasi 2D material

The importance of this dimensional aspect lies in its capacity to reveal newly identified extraordinary phenomena in quasi-2D materials with thicknesses extending up to a nanometer, phenomena absent in their 3D equivalents. Low-dimensional materials showcase unique optical, mechanical, magnetic, and electrical characteristics, rendering them compelling subjects for investigation(1). Moreover, owing to their reduced size, they present ideal candidates for semiconductor chip fabrication and advancements in nanotechnology.

### 1.2.2 2D van der Waals Materials

Layered materials that have strong intra-layer bonding and weak (van der Waals) interlayer bonding are called van der Waals (vdW) materials. They are used to obtain two-dimensional (2D) materials, which are a few nanometers in thickness.

2D materials can be made using a top-down approach like exfoliation or a bottom-up approach like chemical vapor deposition. 2D materials have novel properties than their 3D counterparts, such as high carrier mobility, good thermal conductivity, and high flexibility. These interesting properties of 2D materials make them a promising candidate for constructing various electronic,

valley-tronic, and optoelectronic nano-devices.(2) Since the exfoliation of graphene (graphite mono-layer) in 2004 using scotch tape, the interest in studying these 2D van der-waal materials has bloomed. These materials provide a great flexibility in tuning physical and chemical properties of the material by engineering defects, twist, ion intercalation, substitution, gating, inducing proximity effects and strain etc.

## 1.3 2D Magnets and related emergent phenomena's

Magnetism is most common phenomena that is observed in nature that originates from motion of electrons in matter. The spin and orbital angular momentum of electrons couples with nucleus magnetic moment giving rising to magnetism. Magnetism is essentially at low temperature phenomena where thermal fluctuation is not strong enough to destroy spin alignment.(3,4)

After 2016, 2D magnets have become an emerging field of research to study the quantum hall effect, giant magnetoresistance, spin polarisation, etc. the most fundamental phenomenon that is in play is exchange interaction and spin-orbit coupling (SOC).

The essence of magnetism research lies in understanding the interplay between exchange interaction, spin-orbit coupling, and the Zeeman effect. These factors collectively account for the organization of spins, orbital moments, and magneto-crystalline anisotropy, as well as the influence of external fields on these properties. At the heart of this study are interatomic or interelectronic exchange interactions, which underpin the phenomenon of long-range magnetic ordering. Such ordering manifests in the form of parallel and antiparallel spin arrangements, characterizing ferromagnetic (FM) and antiferromagnetic (AFM) orders respectively, over extended distances.

As dimensional size decreases, there is generally a rise in the magnetic moment per atom. This increase can be explained by factors such as reduced coordination number, the quantum confinement effect, and decreased quenching of the orbital magnetic moment. Compared to 3D magnetic system, the decrease in spatial dimension cause significant thermal fluctuations in 2D magnetic system resulting more complex magnetic system. Based on the magnetic ions' type and electronic band structures, various traditional exchange mechanisms, such as: -

- Direct-exchange interaction (5)
- Super-exchange interaction
- Double exchange interaction
- Itinerant electrons (STONER MODEL)
- Ruderman-Kittel-Kasuya-Yosida (RKKY) mechanisms

are all found in various 2D systems, in addition three novel and intriguing exchange interaction mechanism have also been identified: -

- Super-Exchange interaction
- Extended - Exchange Interaction
- Multi-intermediate Exchange Interaction

According to the Mermin-Wagner theorem(6), two-dimensional (2D) magnetic systems cannot exhibit long-range ferromagnetic (FM) or antiferromagnetic (AFM) ordering at T > 0K for the isotropic Heisenberg model. However, magnetism persists due to factors such as magneto-crystalline anisotropy and dipolar interaction. Despite these interactions having relatively low strengths, typically around 1meV, they play a crucial role in 2D materials by disrupting the conditions set by the Mermin-Wagner theorem.(7–10)

Emergent phenomena such Quantum Hall effect(11), Kondo effect, Topological spin textures (Skyrmions), Topological defects such as change from surface states to edge states are found in 2D Magnets.(12)

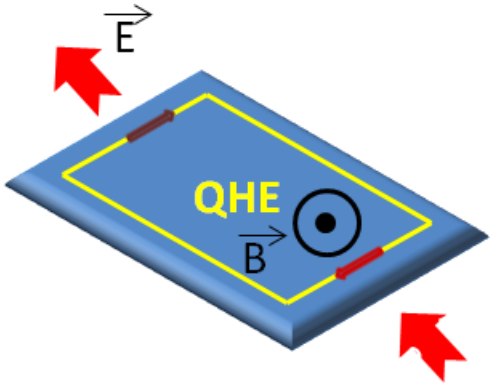


Figure 1.2: Schematic diagram of Quantum Hall effect

## 1.4 Outline of thesis

The thesis is written in a way so as to incorporate an overview of the methods followed for various types of experiments which will be helpful for students and researchers new in the field. I have tried my best to keep the language as simple as possible and get technical wherever necessary.

**Chapter 2** gives information regarding the class material being studied in this thesis. **Description regarding sample $MnPS_3$ and CrSBr** and **Motivation** regarding the experiment. **Chapter 3** contains the working principle **of Scanning Tunneling Microscope** and **Atomic force microscope**. **Chapter 4** is based on **Characterization of the sample using Optical Microscope, Atomic force Microscopy and Raman Spectroscopy and HR-TEM**. **Chapter 5** discuss about LT-UHV STM and Instruments. **Chapter 6** discuss on **STM experiment done on CrSBr and defect probing**. In **Chapter 7,** obtained UV-VIS optical response of material $MnPS_3$ using reflectance and transmittance setup and calculated optical band gap at room temperature. **Chapter 8** discusses the summary of the thesis and future plans.

# Chapter 2 About Material: $MnPS_3$ and CrSBr

## 2.1 $MnPS_3$

Since its synthesis by Barry E. Taylor in 1973(13), this vdW material has been widely studied in most areas, from intercalation, substitution, ferroelectricity, and Heisenberg anti-ferromagnetism to the fabrication of dilute magnetic semiconductors. This material belongs to the one least explored vdW family of material that is of transition-metal phosphorus tri-sulfides ($MPX_3$) in its 2-dimensional regime.

In 2015, Xiong et al.(14) initially observed thermochemically fabricated 2D sheets of $FePS_3$ and $MnPS_3$ within the $MPS_3$ family, ultimately achieving monolayer $FePS_3$. Shortly thereafter, bulk materials of $NiPS_3$ and $MnPS_3$ were also mechanically exfoliated into 2D nanoflakes in laboratory environments. Consequently, it is reasonable to explore the magnetic characteristics of these materials as well as other stable $MPS_3$ systems at the monolayer threshold.

| | Composition | Magnetic Nature | Neel Temperature | μ per metal atom (in $\mu_B$) |
|---|---|---|---|---|
| Transition Metal Phosphorus tri-sulfide ($MPS_3$) | $MnPS_3$ | Neel Heisenberg AFM | 78K | 5.90 |
| | $FePS_3$ | Ising-Zig Zag AFM | 123K | 5.67 |
| | $NiPS_3$ | XY-stripy AFM | 155K | 2.97 |

Table 2.1: Magnetic properties of $MPS_3$ Family – Left column shows the different $MPS_3$ material composition and right column shows the magnetic properties the material

$MnPS_3$ have Type II Heisenberg Neel anti-ferromagnetically (Mn atoms are anti-ferromagnetically coupled with neighbor Mn atoms within the layer and inter-layer ferromagnetic coupled with Mn atoms) order below the Neel temperature ($T_N$) at zero field, which is approximately 78 K, (with the spins of the manganese atoms ordering within individual layers and pointing nearly perpendicularly to them due to an easy-axis out-of-plane anisotropy along c axis). It has a yellowish-green color as shown figure 2.2.(15–18)

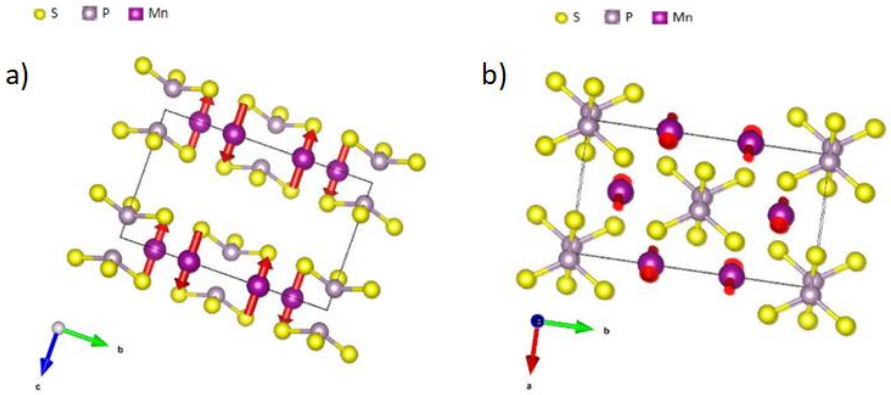


Figure 2.1: Crystal Structure of $MnPS_3$. (a) Side view of the unit cell of $MnPS_3$ .(b) Top view of unit cell of $MnPS_3$

The top and side view of $MnPS_3$ is shown in figure (2.1). Each unit cell of $MPS_3$ is composed of two Mn cations and one $[P_2S_6]^{4-}$ cluster. The Mn atoms are surrounded by six S atoms, while the P atoms are surrounded by three S atoms and one P atom, resulting in the formation of a $[P_2S_6]^{4-}$ anion, which adopts a 2D honeycomb structure. Due to the presence of surface S atoms, $MPS_3$ layers display significant van der Waals characteristics, facilitating easy exfoliation from the bulk phase. A unit cell possessing lattice parameters typical of MnPS3, with dimensions a = 6.07 Å, b = 10.524 Å, c = 6.796 Å, and an angle $\beta = 107.35^{o}$. Hence, the c-axis is not quite parallel to the z-direction.

$MnPS_3$ is a semiconductor with a high band gap of 2.64eV. It has been found that the Magnetic properties of $MnPS_3$ persist to a monolayer of thickness 0.67 nm. It has a high spin flop field of 5T (perpendicular magnetic field is applied), shows 100% magneto-resistance in monolayer, and decreases as layer number increases(19). The anti-ferromagnetic nature of the material is probed using temperature-dependent Raman spectroscopy(20). Pressure-induced insulator-to-metal transition with an additional decrease in direct band gap and color of the flake was observed. $MnPS_3$ shows no PL signal at room temperature but a PL signal of 940 nm is observed at low temperature(21). Bulk $MnPS_3$ has refractive index of 2.41 but complex refractive index of few layers $MnPS_3$ is still unknown. (22)

Various hetero-structures using $MnPS_3$ have been studied. The transition temperature of $MnPS_3$ was determined using Gr/$MnPS_3$/Gr tunneling current. An Interfacial AFM/FM hetero-structure was studied using FGT/$MnPS_3$ showing anti-symmetric magneto-resistance.(23–26)

Figure2.2: Bulk crystal of $MnPS_3$

## 2.2 CrSBr

One of the newly emerging vdW materials that has the potential to be used in applications such as spintronics and to study fundamental physics such as 2D anti-ferromagnetism is CrSBr. First synthesized by H. Katsher in 1966(27), the material remained highly unexplored until 2019. Due to its high resistance to degradation to air and low dimensional magnetism, it became a fascinating material to explore.

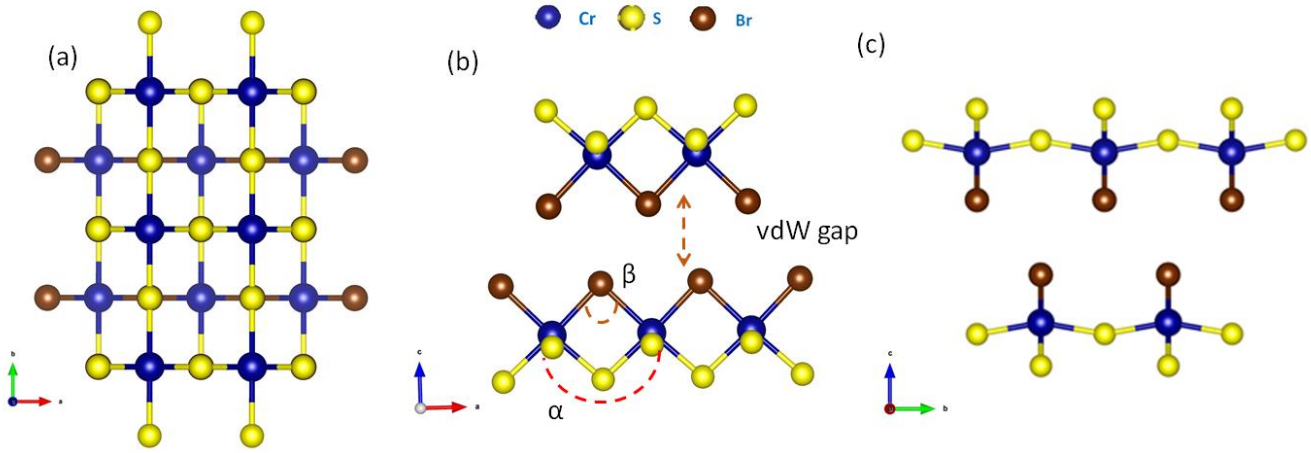


Figure 2.3: Shows the crystal structure of CrSBr (a) Top view (b) and (c) Side view

CrSBr has orthorhombic structure with *Pmmn* space group as shown in figure 2.3. The structure consists of monolayers composed of CrSBr, which is bonded by van der Waals interaction along the c-axis. The monolayer comprised of edge sharing [$CrS_4Br_2$] octahedral units, with an

underlying squared lattice arrangement of Cr (III) cations. The reported data suggest that the lattice parameter of a = 3.5 Å, b = 4.7 Å and c = 7.9 Å. The chemical bonding along the basal directions involves Cr-(S, Br)-Cr paths along the a-axis with a cation-anion-cation angle of $\alpha = 95^{o}$ and $\beta = 90^{o}$.(28)

CrSBr is an A-type anti-ferromagnetic semiconductor with a bulk direct band-gap of approximately 1.5 eV, Neel temperature of 132 K, and Curie temperature of 150 K. The Cr magnetic ions are interlayered antiferromagnetic coupled while in in-plane there is ferromagnetic coupling. It has average sheet resistance $R_s = 240 \pm 60$ KΩ at room temperature. Magnetic property measurements suggest that the b-axis is the magnetic easy axis ($H_{sf}$ = 0.35 T), the c-axis is the magnetic hard axis ($H_{sf}$ = 2 T), and the a-axis is the magnetic intermediate axis ($H_{sf}$ = 1 T). Magneto-resistance measurement shows large negative MRR below $T_N$ up to maximum of -29.3%, -39,2% and -32.7% along a, b and c axes respectively. (29)

Previously reported data of STS on CrSBr shows semiconductor band gap of approximately 1.5 ± 0.2 eV with Fermi level near conduction band suggesting CrSBr sample is unintentionally electron doped due intrinsic Br vacancy. It has also been reported that it has high effective mass anisotropy $m^e_X / m^e_Y \sim 50$ (x and y refers to a and b direction respectively). Conductance along both a and b direction increases linearly temperature up to maximum at 80 K and then decreases to saturate at room temperature. Conductance ratio ($\sigma_b/\sigma_a$) was found to be order $10^2$ (no bias applied to material) and $10^5$ (positive bias applied to material) suggesting quasi 1D electronic transport in 2D semiconductor.(29–31)

## 2.3 Motivation

This thesis is motivated to understand 2D magnets (mainly 2D antiferromagnets) which would help make both magneto-optical device and nano-spintronics devices.

$MnPS_3$ is a layered antiferromagnetic semiconductor material with band gap 2.64eV. It's intralayer Mn atoms ate anti-ferromagnetically coupled and interlayer ferromagnetically coupled. $MnPS_3$ showcases a captivating optical phenomenon, revealing a broad spectrum of colors attributed to thin film interference of its thin nanoflakes. This distinctive characteristic distinguishes $MnPS_3$

from conventional semiconductors, hinting at its potential for groundbreaking applications in optics and beyond. Intrigued by this unique property, this thesis endeavors to delve into the underlying optical behavior of $MnPS_3$, particularly by focusing on the determination of the complex refractive index of few-layer samples. By unraveling the intricacies of light-matter interactions within $MnPS_3$, especially in its paramagnetic phase at room temperature, this research not only seeks to enhance our fundamental understanding of this material but also aims to pave the way for the development of innovative magneto-optical devices.

Another antiferromagnetic material, CrSBr which is a semiconductor with band gap 1.5 eV was also explored in this thesis. In contrast to the previous sample, the presence of intra-layer ferromagnetism and interlayer anti-ferromagnetism renders it the most suitable specimen for comparison with $MnPS_3$. Renowned for its strong 2D electronic anisotropy, CrSBr presents a compelling subject for studying localized electronic behavior and defects. Utilizing scanning tunneling microscopy (STM) measurements conducted at 77 K, this research delves into the electronic behavior and defects within CrSBr. This investigation aims to elucidate the changes in the local density of states around defects and determine the band gap in the defect region. Understanding these phenomena at a microscopic level not only advances our fundamental understanding of this material but also holds promise for the development of novel magnetic and electronic devices.

# Chapter 3 Scanning Probe microscopy

In scanning probe microscopy, a branch of microscopy, a sample's surface is scanned at the nano scale to create an image. This is accomplished using a physical probe that interacts with the sample, scans its surface, and gathers data typically obtained as a 2D grid of data points and displayed on a computer screen. Various probe microscopy techniques are used to obtain topography (the image of the sample) of different types of samples, such as conducting, non-conducting, and biomolecules. The basic idea behind SPM is to raster scan the sample's surface using a sharp tip to provide the topography line by line.

## 3.1 Scanning Tunneling Microscopy (STM)

Scanning Tunneling Microscope (STM) is an instrument that is used to get the imaging of the conducting samples at the atomic level. The instrument can produce a picture of a sample with a resolution of 1˚A and a precision of approximately $10^{-9}$ times its size. The instrument can produce a picture of a sample with a resolution of 1˚A and a precision of approximately $10^{-9}$ times its size.

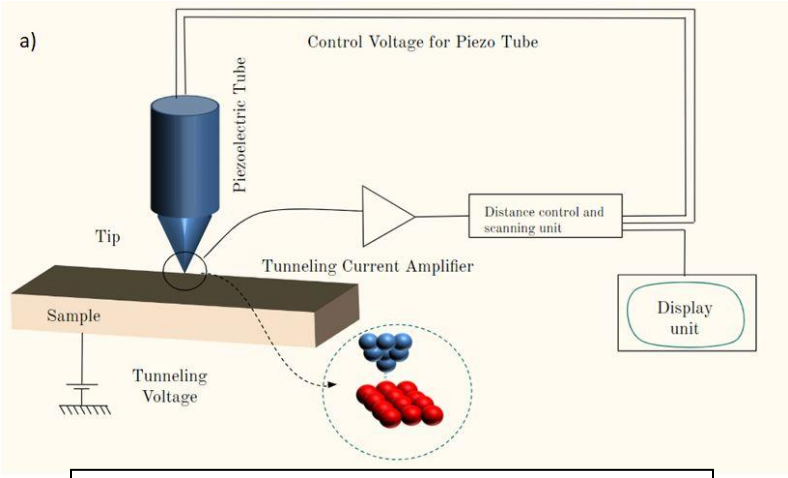


Figure 3.1 Schematic Diagram of STM

A steady power source is connected to the STM setup's system, which includes a metal tip and the sample surface as shown in figure (3.1). The system operates using the tunneling principle of quantum mechanics. The tip is made to apply a slight voltage bias to the sample with respect to the tip, allowing for the detection of tunneling current when it approaches the surface of the sample

at a specific distance. The tip is fixed on piezoelectric material, which uses a feedback loop to maintain both the tip and the sample distance.

The configuration of this setup is such that, during scanning in the x-y plane, any change in the surface height and density of states will be detected by the change in current value. Generally, a 0.1 Å variation in the tip and sample distance results in a 20% change in tunneling current.(32)

STM generally have two modes:

1. Constant Height mode
2. Constant Current mode

**Constant Height mode:** In this scanning mode, the height of the tip over the surface stays constant while the current varies along the x-y plane of scanning to maintain the constant height. This kind of scanning mode produces a picture based on surface current variations that are connected to the density of states. Figure (3.2 a)

**Constant Current Mode:** The height changes in this scanning mode to maintain a steady current. By adjusting the Z-piezo height continuously, the feedback loop helps maintain a constant current by providing a topography of the integrated density of states throughout the sample. Figure (3.2 b)

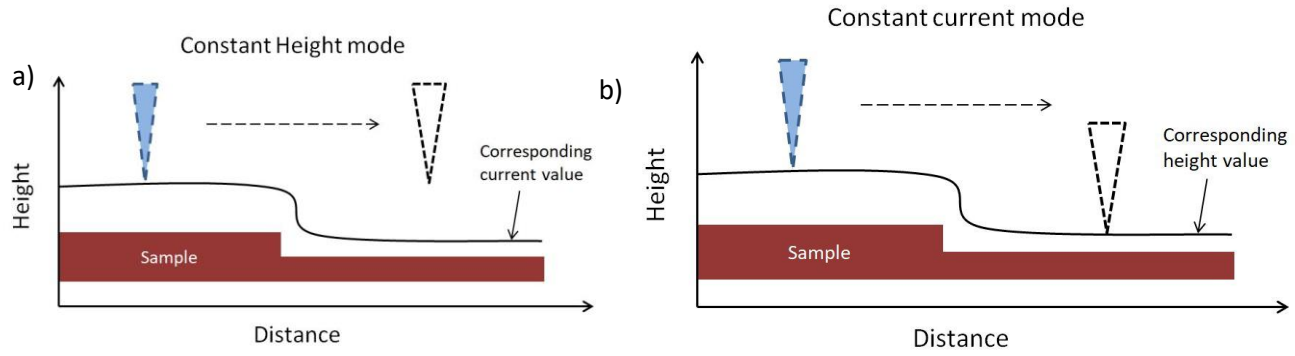


Figure 3.2: (a) STM operating at constant height mode (b) STM operating at constant current mode

## 3.2 Quantum Tunneling

A particle needs enough energy or greater than the potential barrier in the classical regime to be able to pass through it. But in quantum regime, even if the particle energy is less than that of potential barrier there exist a non-zero probability that the particle can enter and pass through the classical forbidden regime. This phenomenon is known as 'Quantum mechanical Tunneling'.

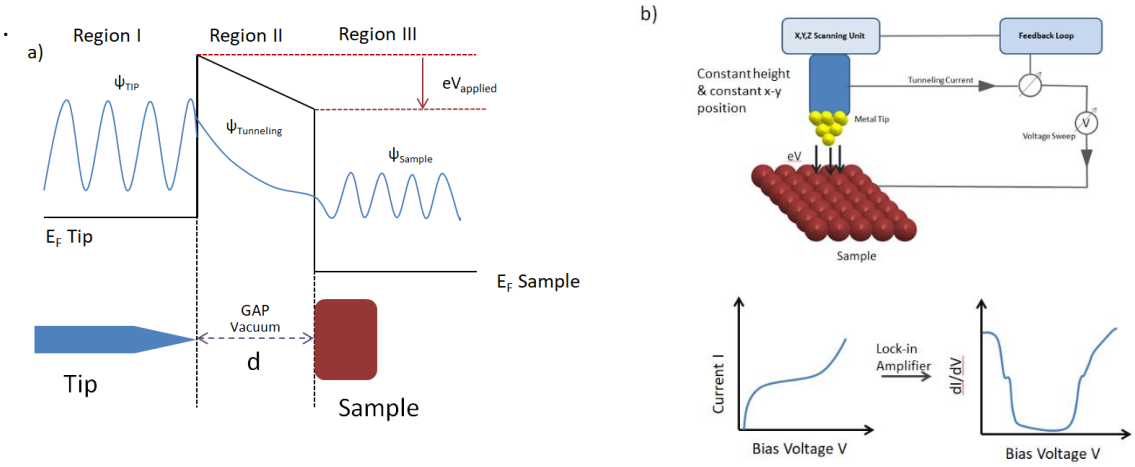


Figure 3.3: (a) 1D schematic diagram of Quantum tunneling of electrons through potential barrier of gap d units. (b) Working Principle for Scanning tunneling Spectroscopy

Figure (3.3 a) shows the wavefunction of the electron and probability amplitude decreases passing through the potential barrier (classical forbidden region) , but the energy energy assosciated with the wavefunction remain constant. In the case of the STM, the gap between the tip and the sample act as forbidden regime which is vaccum and electrons tunnels through it giving tunneling current.The energy of the electrons after they pass through determines the value of current. Tunneling current falls when the barrier gap rises and vice versa.

The electron in the solid occupies the highest energy level known as the Fermi level with energy $E = E_{\text{particle}}$. However, the energy of the electron at the Fermi level is lesser than that of the vacuum.

The exponential decay of wave function of the electron inside the gap is given by:

$$\psi_{(}Z) = \psi e^{-\kappa Z}$$

The above equation is a solution of Schrodinger equation. (32)

## 3.3 Bardeen theory of Tunneling

Quantum Tunneling is a fundamental phenomenon in Quantum mechanics. According to Bardeen, the tunneling current is the result of numerous separate scattering events working together to move electrons across the tunneling barrier. Bardeen's first-order perturbation theory is used in solids and STM.

Bardeen demonstrated that by possessing sufficient understanding of the electronic properties of both the sample and the tip, it becomes feasible to estimate the rates of individual scattering occurrences during electron tunneling. This analysis leads to the formulation of an expression for the tunneling current, which is determined as the product of the electron charge (e) and the net rate of electron transfer between the tip and the sample. Assumption is taken into account in Bardeen's theory as follows:

- tip and sample state are nearly orthogonal.
- tunneling is weak enough for first-order perturbation.
- The occupation probabilities for both the tip and sample remain unchanged and independent of each other throughout the tunneling process.
- the electron-electron interaction can be neglected.
- the tip and sample are in electrochemical equilibrium with respect to each other.

Bardeen showed this by calculating the tunneling current between two electrodes A and B. when the electrodes A and B are far apart, the wave function of each satisfies the Schrodinger equation for free electrode:

$$i\hbar\frac{\partial\psi}{\partial t} = \left[-\frac{\hbar^2}{2m}\frac{\partial^2}{\partial Z^2} + U\right]\psi$$

U = $U_A$ is the potential for the electrode A and the stationary wave functions:

$$\psi = \psi_\mu e^{-iE_\mu t/\hbar}$$

U = $U_B$ is the potential for the electrode B and the stationary wave functions:

$$\psi = \psi_\nu e^{-iE_\nu t/\hbar}$$

Spatial wave function and energy eigenvalues satisfying:

$$\left[-\frac{\hbar^2}{2m}\frac{\partial^2}{\partial Z^2} + U_i\right]\psi_i = E_i\psi_i$$

where i is either A or B.

When we bring two electrodes close enough so that an electron can tunnel from one to the other, the wavefunctions of the two electrodes will decay into the vacuum,

$$i\hbar\frac{\partial\psi}{\partial t} = \left[-\frac{\hbar^2}{2m}\frac{\partial^2}{\partial Z^2} + U_A + U_B\right]\psi$$

By assuming an ansatz for the above expression:

$$\Psi = \psi_\mu e^{-iE_\mu t/\hbar} + \sum_{\nu=1}^{\infty} c_\nu(t)\chi_\nu e^{-iE_\nu t/\hbar}$$

The tunneling Matrix element $M_{\mu\nu}$ $= \int_{Z>Z_O} \psi_\mu U_B \chi_\nu^* \, dx$

Using the tunneling matrix we can find out the tunneling current (I) and the tunneling Conductance (G)

$$I = \frac{2\pi e^2}{\hbar}|M_{\mu\nu}|^2\rho_B(E_F)\rho_A(E_F)V$$

$$G = 2\pi^2 G_o|M_{\mu\nu}|^2\rho_B(E_F)\rho_A(E_F)V$$

where $G_o$ = 77.48 µS which is quantum conductance.

## 3.4 Tunneling Spectroscopy

Tunneling Current at the bias Voltage V is the summation of all the relevant states present at that energy level. At finite temperature, electrons will follow the Fermi distribution and give tunneling current expression:

$$I = \frac{4\pi e}{\hbar} \int_0^{eV} \rho_A(E_F - eV + \epsilon)\rho_B(E_F + \epsilon)\ d\epsilon$$

The tunneling current I is directly proportional to the integral of the density of states (DOS) from Fermi level to eV, which can be expressed by taking the derivative of DOS of the sample ($\rho_s$) at given eV as :

$$\frac{dI}{dV} = \rho_s(eV)$$

Scanning tunneling spectroscopy (STS) provides information regarding the density of states as a function of energy. The working principle is shown in the Figure 3.3 (b & c). The tip is kept fixed at a particular x-y position and a constant height is maintained by turning the feedback loop off. Then a sweeping voltage is applied and the corresponding I-V curve is recorded. the first derivative of this curve (dI/dV) - V is directly proportional to the local density of states of electrons in the region just below the tip. By setting $N*N$ grid points we spatially visualize the surface DOS by taking dI/dV at each grid point.

## 3.5 Atomic force Microscopy

Atomic force Microscopy is a technique used to obtain the topography of a sample i.e. a description of the physical shape of the surface of the sample at the nano-scale. It works on the principle of measuring the interatomic force between the sample and the cantilever tip to describe the topography of the sample.

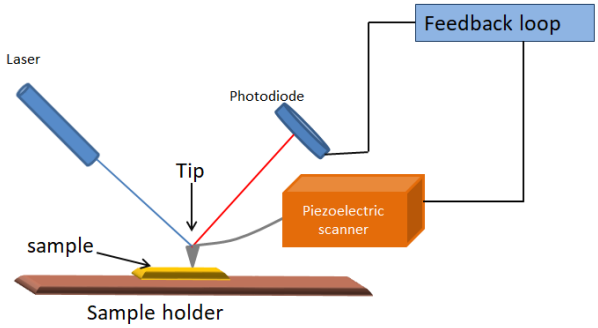


Figure 3.4: Schematic diagram of Atomic Force Microscope

Above figure 3.4 shows a schematic diagram of atomic for Microscope. As shown in the setup, there is cantilever attached to piezoelectric scanner. A sharp tip is attached to the one end of the cantilever which remain suspended over the sample. Any attractive or repulsive force experienced by the tip while scanning the surface changes the defection of cantilever lead change in direction of reflected laser beam on the photo diode detector. The change in deflection on the detection act as feedback signal to piezoelectric scanner.

The AFM operates in 2 modes:

1. **Contact Mode (Static mode**): In this mode, feedback unit controller keeps the deflection constant by adjusting the height of the cantilever. Usually in this mode the force between the cantilever tip and the sample surface is repulsive.
2. **Dynamic mode (Tapping mode):** In this mode, the cantilever oscillates at particular frequency in the range several kilohertz over the sample surface such that the cantilever experience small magnitude of force. The feedback loop keeps the oscillating frequency constant to maintain a constant interacting repulsive force between tip and sample surface.

All the atomic force microscopy experiment was done in the dynamic mode using Tap 190 AL-G cantilever tip.(32)

# Chapter 4 Characterization of Exfoliated $MnPS_3$ and CrSBr

We characterized the exfoliated $MnPS_3$ and CrSBr using compound microscope to estimate it the size and thickness of the flakes with help optical contrast with respect to substrate. Here we have exfoliated $MnPS_3$ and CrSBr using clean room tape on to $SiO_2$/Si substrate then using Atomic force microscopy we determined the thickness of the those nanoflakes and Raman spectroscopy . All the Raman spectroscopy experiments were performed at room temperature Raman spectroscopic data were collected using a 532 nm excitation laser with a beam spot of 2 µm and laser power of 50 mW. Raman data were collected using 50x and 100x objective lenses for $MnPS_3$ and CrSBr respectively. We have also determined the composition of CrSBr using HR-TEM.

## 4.1 $MnPS_3$ characterization

First we start by discussing the characterization of $MnPS_3$ flakes. $MnPS_3$ was exfoliated using blue clean room tape onto three different $SiO_2$/Si substrate of different thickness (0nm $SiO_2$, 90 nm $SiO_2$ and 285nm $SiO_2$).

Thin flakes with broad range of color spectrum were observed as shown in the figure 4.1.

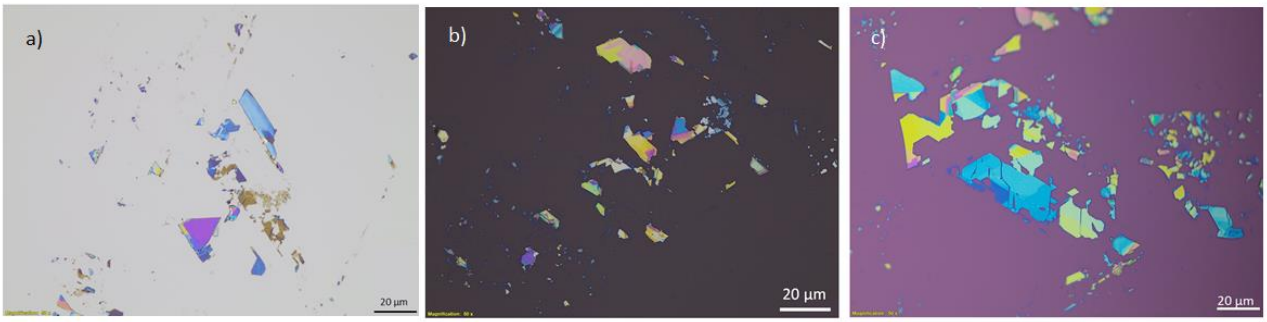


Figure 4.1: Exfoliated Sample of $MnPS_3$ on (a) pure Si substrate (b) 90nm $SiO_2$/Si substrate (c) 285 nm $SiO_2$/Si Substrate

To measure the colors of the $MnPS_3$ flakes accurately, we utilized an image analysis software named ImageJ to extract the 8-bit RGB color values from optical images. Additionally, the height profile of the flakes was determined using a Nanosurf Atomic Force Microscope in Dynamic Mode.

Figure 4.3 depicts the oscillation of RGB values as a function of thickness. We observed that the RGB values exhibit quasi-sinusoidal changes with thickness, with periodicities estimated to be approximately 113 nm for red, 100 nm for green, and 78 nm for blue amplitudes across all three substrates. Additionally, the peak-to-peak amplitude decreases with increasing thickness for each color value. The interference pattern was derived from data collected on various substrates, as illustrated in Figure 4.2.

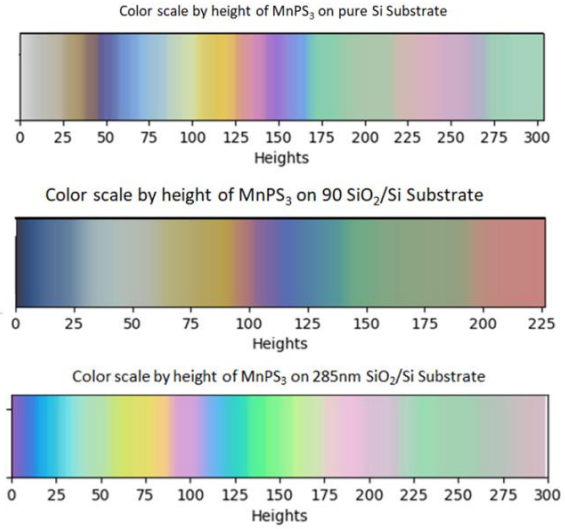


Figure 4.2: Observed Thin film interference of $MnPS_3$ on pure Si substrate, 90nm $SiO_2$/Si substrate ,285 nm $SiO_2$/Si Substrate

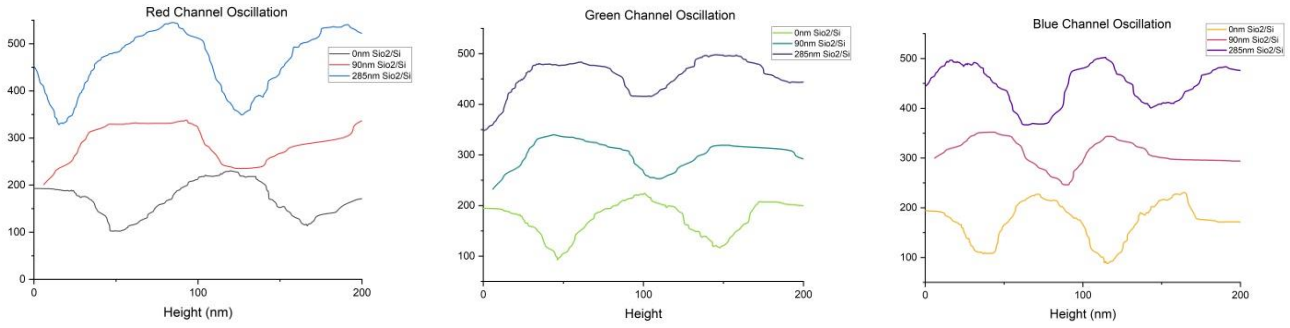


Figure 4.3: Shows Red, Green, Blue channel oscillation and phase difference due to thickness of $SiO_2$

The Optical contrast is low for few layers $MnPS_3$ so to determine the number layers we obtained the height profile of the flakes and characterized them with Raman Spectrum.

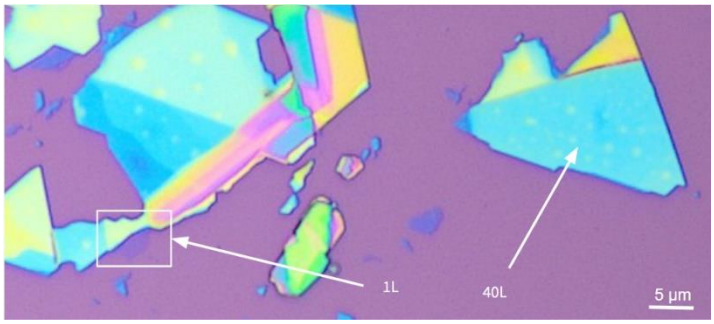


Figure 4.4: 1L(1.18nm) and 40L(27.17nm) $MnPS_3$ on 285nm $SiO_2$/Si

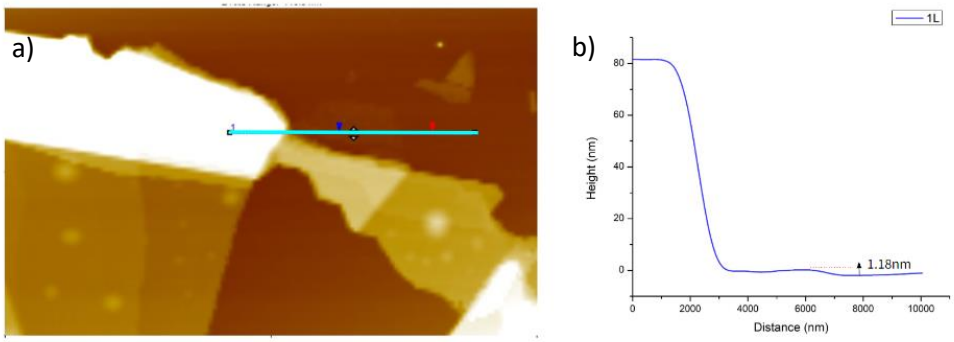


Figure 4.5: $MnPS_3$ 1 Layers AFM image and height profile

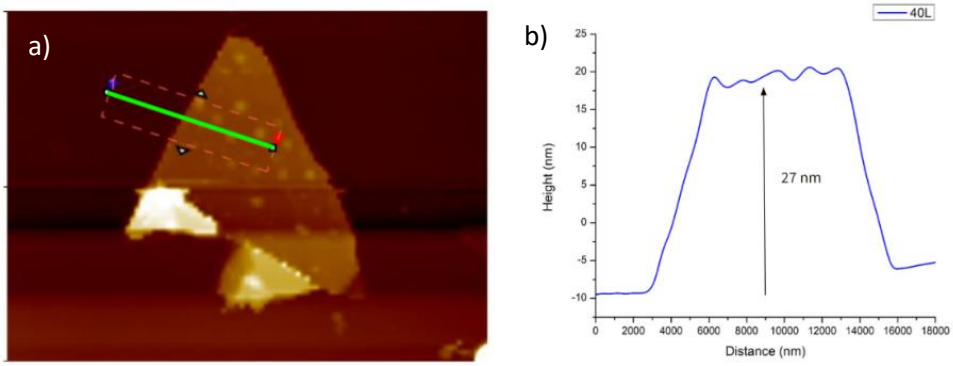


Figure 4.6: $MnPS_3$ 40 Layers AFM image and height profile

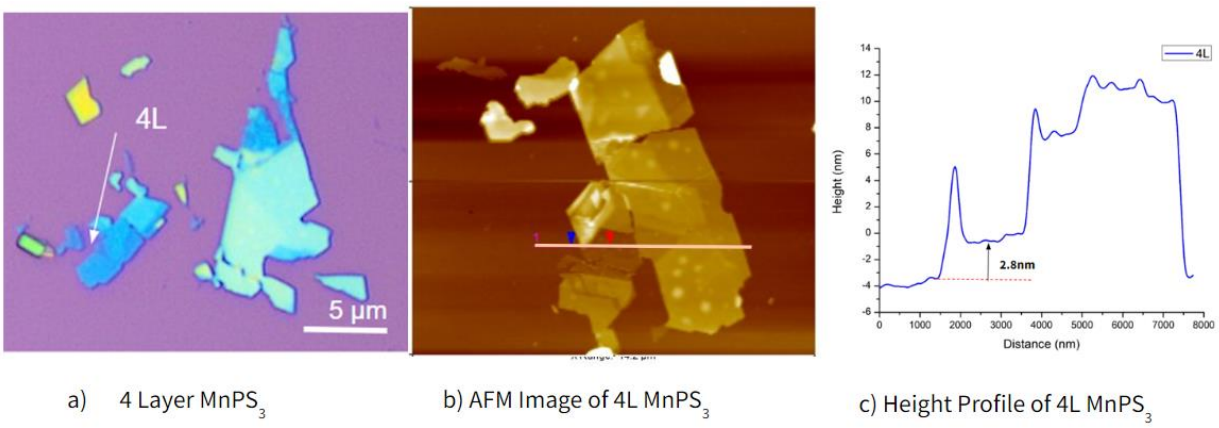


a) 4 Layer $MnPS_3$ b) AFM Image of 4L $MnPS_3$ c) Height Profile of 4L $MnPS_3$

Figure 4.7: $MnPS_3$ 4 Layers (a) Optical image, (b) AFM image and (c) height profile

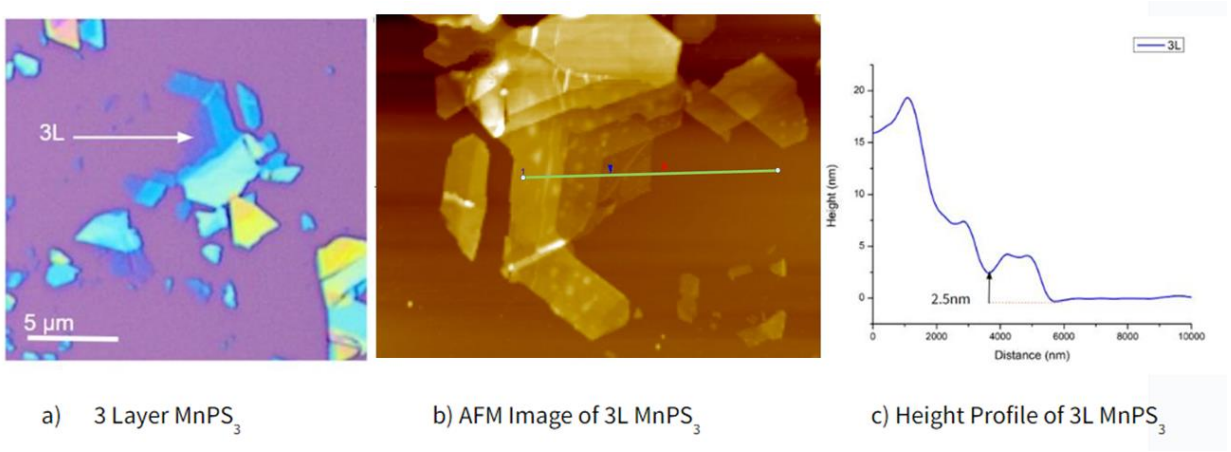


a) 3 Layer $MnPS_3$ b) AFM Image of 3L $MnPS_3$ c) Height Profile of 3L $MnPS_3$

Figure 4.8: $MnPS_3$ 3 Layers (a) Optical image, (b) AFM image and (c) height profile

The figure below shows layer-dependent Raman characterization of $MnPS_3$ flakes.

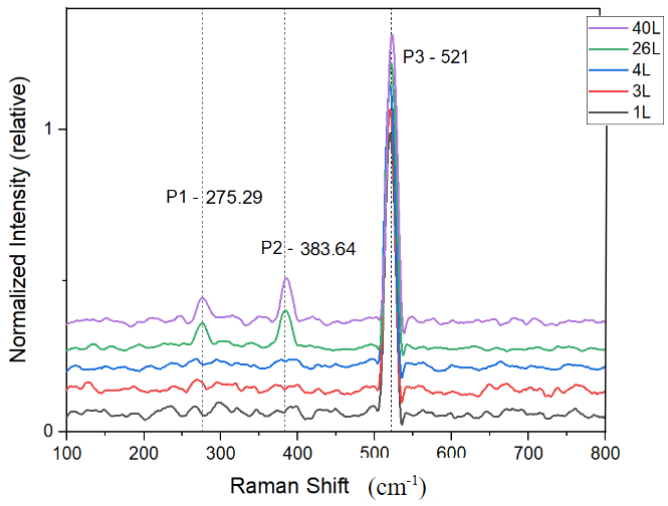


Figure 4.9: $MnPS_3$ Raman peaks

The characteristic Raman peaks of $MnPS_3$ at $P_1$ = 275.29 $cm^{-1}$ ($E_g$) and $P_2$ =383.64cm-1 ($A_g$) was observed which are previously reported. The monolayer shows no characteristic peaks whereas the bulk $MnPS_3$ shows peaks at $P_1$ and $P_2$. There are also other peaks that reported But in contrast, no peaks were observed for the 3 and 4-layer $MnPS_3$. The peak $P_3$ = 521$cm^{-1}$ represent Raman peak of $SiO_2$.(20)

Increase in peak intensity and no peaks in few layer $MnPS_3$ suggest , as the dimensionality increases the phonon normal modes are enhanced due increases in intra-layer coupling.

## 4.2 CrSBr characterization

### 4.2.1 Optical, AFM, Raman characterization of CrSBr

CrSBr was exfoliated using blue clean room tape onto 285nm $SiO_2$ as shown in the figure (4.8). Most of the thin flakes has rectangular shape. Length represents the a-direction and breadth represents b-direction of the CrSBr flakes.

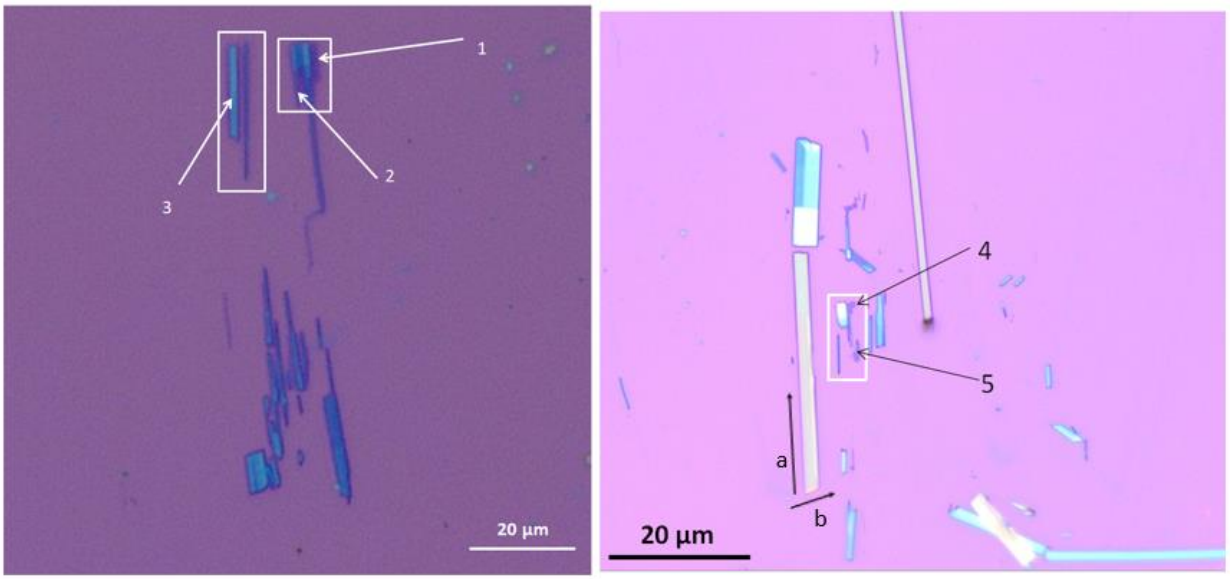


Figure 4.10: Exfoliated Sample of CrSBr on 285nm $SiO_2$/Si substrate

Identifying few layer CrSBr flakes directly from optical contrast is difficult. So, I have characterized the flakes based upon its height and Raman spectroscopy.

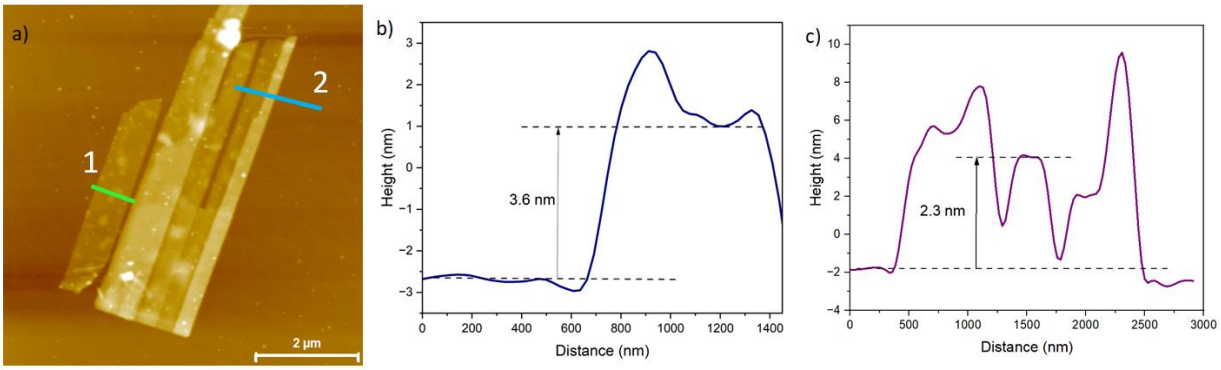


Figure 4.11: (a) AFM image of 4L and 3L CrSBr (b) and (c) shows the height profile

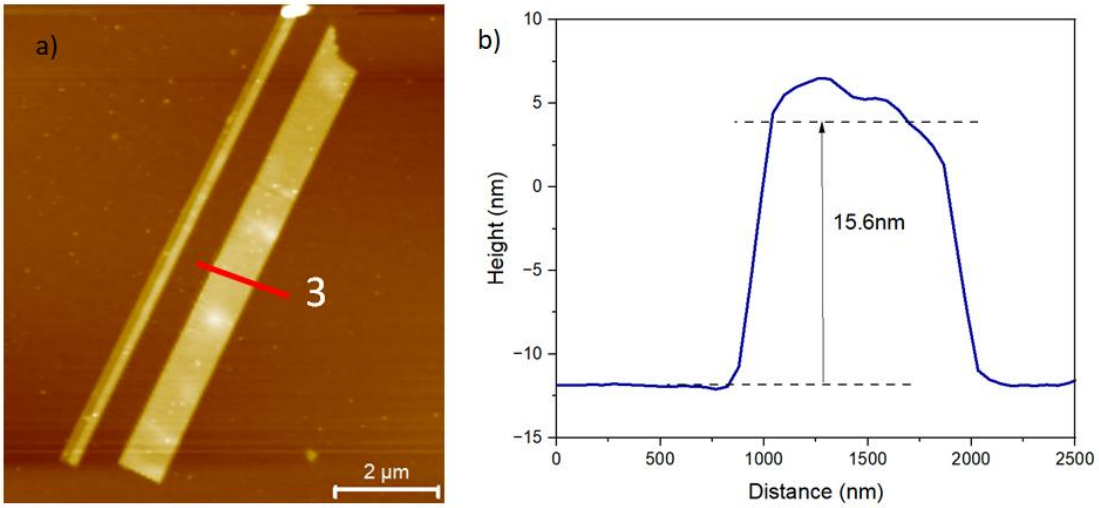


Figure 4.12: (a) AFM image of 20 L CrSBr (b) shows the height profile

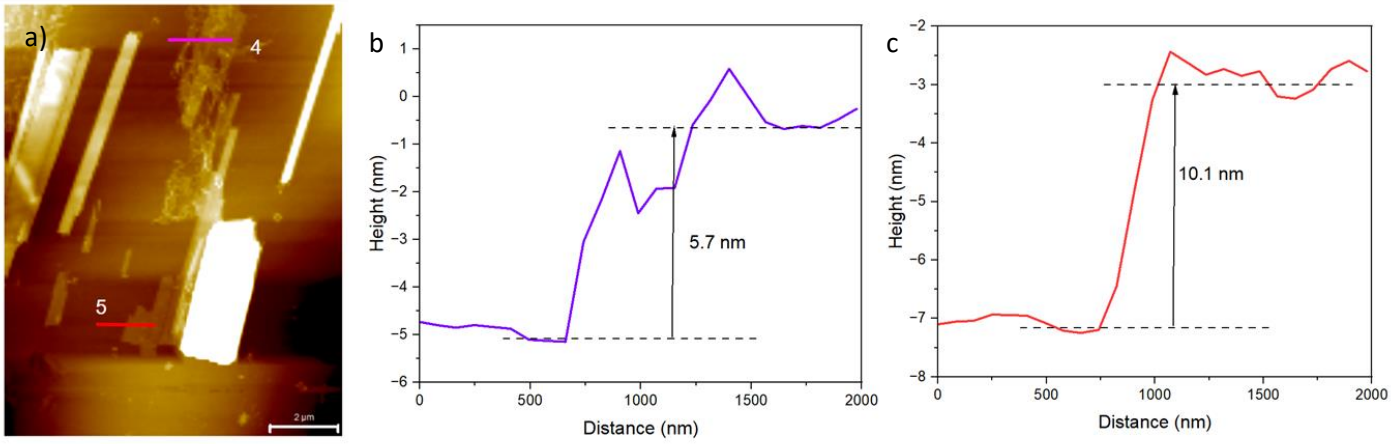


Figure 4.13: (a) AFM image of 7L and 12L CrSBr (b) and (c) shows the height profile

The above figure 4.11, 4.12, 4.13 shows the AFM images and height profile thin CrSBr flakes.

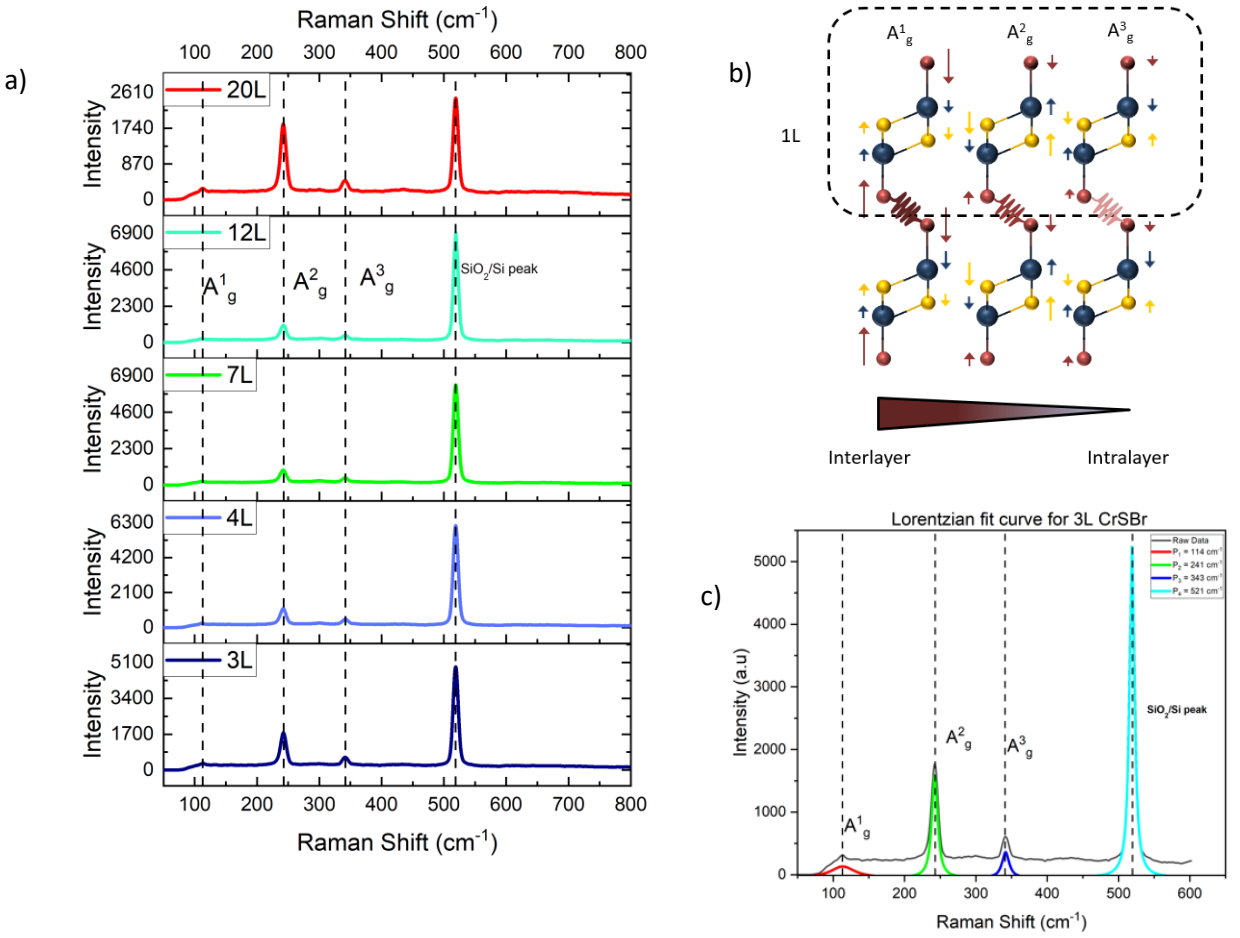


**Figure 4.14:** a) Shows the layer dependent Raman peaks b) The atomic displacements of the three Raman active Ag modes in 1L CrSBr, with two layers stacked to demonstrate interlayer coupling. The $A^1_g$ and $A^2_g$ modes are influenced by bromine atoms, facilitating vibrational interlayer coupling, while the $A^3_g$ mode exhibits minimal bromine contribution and consequently low interlayer coupling(33). c) Lorentzian fit for the 3L CrSBr shows the 3 Out of plane vibrational modes.

Figure 4.14 (a) shows the Raman peaks of the exfoliated CrSBr with 3, 4 ,7 ,12, 20 mono layers. All the three modes are out of plane vibrational modes. **$A^1_g$ = 114 $cm^{-1}$, $A^2_g$ = 244$cm^{-1}$, $A^3_g$ = 344 $cm^{-1}$**. It has been reported that $A^1_g$ and $A^3_g$ are polarized along b-axis whereas $A^2_g$ is polarized along a-axis. Figure 4.12 b) shows the atomic displacement of atoms during vibration in 3 different normal modes. The $A^1_g$ and $A^2_g$ mode frequency are layer- dependent. With decreasing number of layers those two mode frequency decreases showing energy red shift where as the $A^3_g$ mode is layer independent. Bromine atoms, positioned within the outer layers of each covalently bonded monolayer, serve as mediators for the vibrational interlayer coupling among the layers. It is a common observation that Raman peaks exhibit stiffening as the layer number increases, attributable to heightened interlayer vibrational interactions leading to a large restoring force. This is particularly evident in the $A^3_g$ mode, which displays minimal change.(33)

### 4.2.2 HR-TEM of CrSBr

High resolution – Transmission electron Microscope used to characterize CrSBr crystal to find the vacancy concentration Figure 4.15 (a) shows the HR-TEM image of one of the exfoliated CrSBr nanosheets using the ultrasonication method in IPA solution. Using elemental mapping, stoichiometry of the CrSBr crystal was extracted and result of their concentration are shown in Figure 4.15 (b), Figure 4.15 (c) and Figure 4.15 (d).

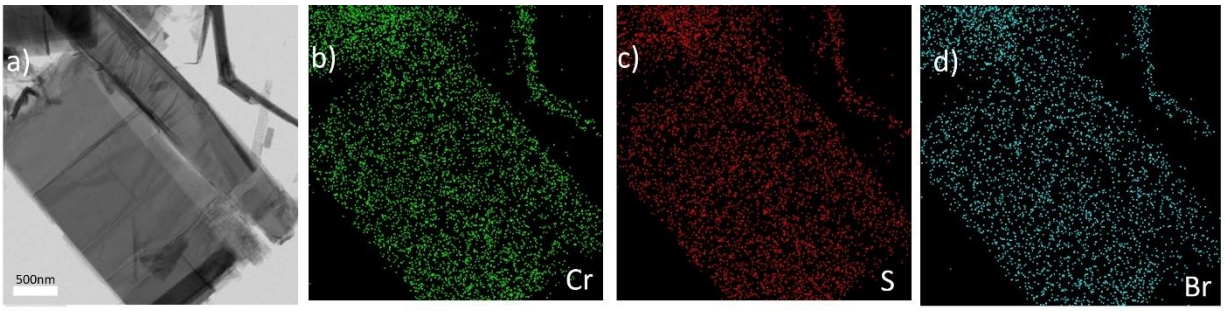


Figure 4.15: HR-TEM and Elemental Mapping of Fe-intercalated CrSBr. (a) HR-TEM image of a typical CrSBr nanoflake. (b) Elemental mapping of Cr. (c) Elemental mapping of S.(d) Elemental mapping of Br.

Elemental analysis of various flakes was conducted, a summarized table is shown in table 4.1. Typical CrSBr has Br vacancy and Cr concentration is as taken 1. But in our case, we found the empirical formula for the sample as **$Cr_{0.67}S_{0.53}Br$** shows high concentration of Cr and S vacancy is present along low concentration of Br vacancy.(34)

| Elemental Mapping | Cr | S | Br |
|---|---|---|---|
| Atomic percentage | 30.48 | 24.38 | 45.24 |
| | 30.34 | 24.29 | 45.38 |
| | 31.17 | 24.87 | 43.97 |

Table 4.1: Elemental Mapping of CrSBr. The three column shows the atomic percentage of each element in CrSBr

# Chapter 5 LT-STM and Instrumentation

All STM measurements were performed in the Scientia Omicron Low-temperature ultra-high vacuum STM. The figure shows the setup. There are 3 main sections of the system: LT-STM Chamber, Preparation chamber and load lock Chamber, each operating at different vacuum pressure condition and separated by valves. Samples and tips are moved across each chamber using a magnetic wobble stick.

## 5.1 LT-STM Chamber

LT-STM Chamber has two cylinders: lower cylinder and upper cylinder. The Lower cylinder is generally empty and the upper cylinder chamber has two coaxial cylinders equipped with a bath cryostat for liquid nitrogen ($LN_2$) and liquid Helium (LHe) which enables the system to work over range of temperature (4.3K - 300K). Heater is present under the sample which works using feedback loop to maintain the temperature of the system at particular temperature. LT-STM chamber has a base pressure of 2 x $10^{-9}$ mbar can reach up to $10^{-11}$ mbar. For vibration isolation, the tip-sample assembly is attached to a sample holder that is suspended by a spring.

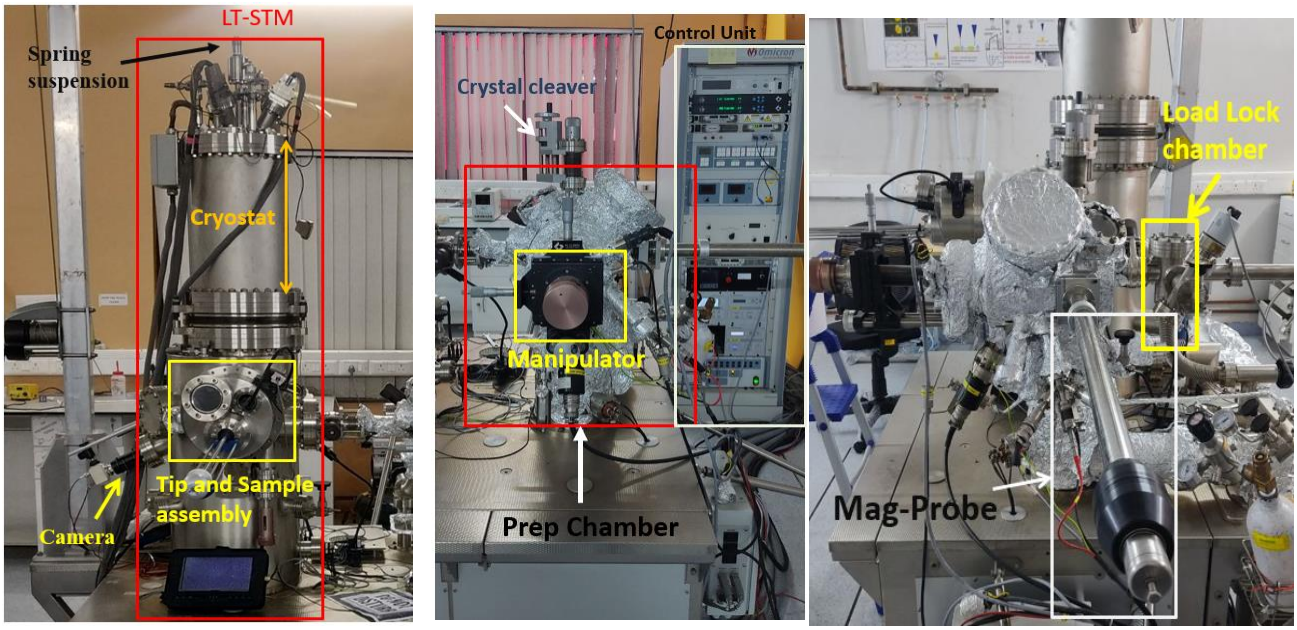


Figure 5.1: (a) LT-UHV STM chamber (b) Preparation Chamber (c) Load Lock chamber

This spring has three positions

(i) cooling position in which the assembly is in contact with cryostat for fast cooling.

(ii) bake-out position is used during baking of the system.

(iii) scanning position while taking measurements.

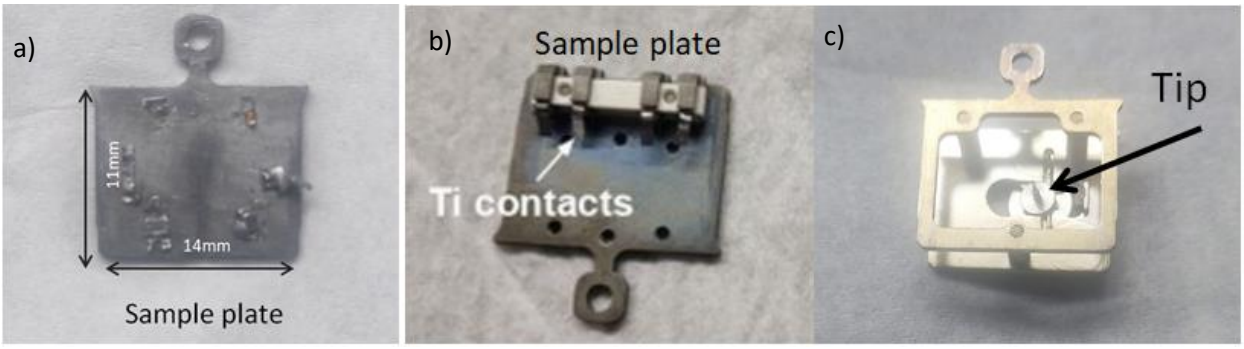


Figure 5.2: (a) Normal STM plate, (b) Four Probe Sample plate with Ti contact, (c) STM Tip Holder

## 5.2 Preparation Chamber and Load Lock Chamber

All sample and tips are first transferred into the load lock chamber then using the mag probe, both sample and tip are transferred into the preparation chamber. Load lock chamber is maintained at atomic pressure to transfer the sample from air to load lock chamber. Then load lock chamber is brought to pressure of $10^{-7}$ mbar and then sample transferred to preparation chamber. The preparation chamber is equipped with a sputtering system for cleaning sample and resistive heater for annealing samples. It is also equipped with e-beam evaporator for in-situ sample deposition and a crystal cleaver for in-situ exfoliation of samples. The Prep chamber has a base vacuum of $10^{-8}$ mbar.

## 5.3 Sample plates and tip Holder

Three-types plates are used in the system.

1. Normal Sample plate for STM measurement shown in figure 5.2 (a).
2. 4 probe sample plate for transport shown in figure 5.2 (b). It is transport sample plate with 4 titanium contacts

3. Tip holder for STM tips shown in figure 5.2 (c). Tungsten tip is attached to the tip holder via magnet which is coupled to the piezoelectric scanner in the LT-STM chamber.

All sample plates are made up of Molybdenum.

## 5.4 Vacuum Pumps

There are 4 types of vacuum pumps attached to the system: Rotary pump, Turbo molecular pump, Ion pump, and Titanium sublimation pump (TSP). The rotary pump creates a vacuum pressure of $10^{-3}$ mbar after that turbo-molecular pump starts bring the system to vacuum pressure of $10^{-9}$ mbar. Next ion pump continues to maintain the pressure as turbo-molecular pump is switched off during the scanning to avoid noise. TSP pump is used occasionally to remove the adsorbents from inner surface of the chamber.

LT-chamber is connected to one set of all four pumps and prep chamber is connected to second set of vacuum pumps. Load-lock chamber is only connected to rotary and turbo-molecular pump. Pressure gauge such as the Pirani gauge and ion gauge are used to monitor the pressure in Load lock (former) and LT-STM, Prep chamber (later) separately.

## 5.5 STM Sample preparation

The STM plate was first polished using high grade sandpaper to flat the surface and then sonicated in acetone and cleaned using IPA. CrSBr bulk Crystal was mounted on the STM sample plate using silver epoxy as a conducting adhesive material shown in the figure 5.3(a). Then it is curated at 150$^{o}$C for 1.5 hours at vacuum of $10^{-6}$ mbar pressure to avoid sample degradation. Then the sample was exfoliated using highly adhesive green clean room tape, figure 5.3 (b and c) shows both un-cleaved and cleaved sample. The sample was transferred from load lock chamber to prep chamber then finally into LT STM chamber where all STM measurements were performed at base pressure 2 x $10^{-9}$ mbar and a temperature of 77K.


Figure 5.3: (a) Bulk Crystal on STM sample plate attached using silver epoxy, (b) Un-cleaved CrSBr crystal, (c) Cleaved CrSBr crystal.

# Chapter 6 Defect Study on CrSBr

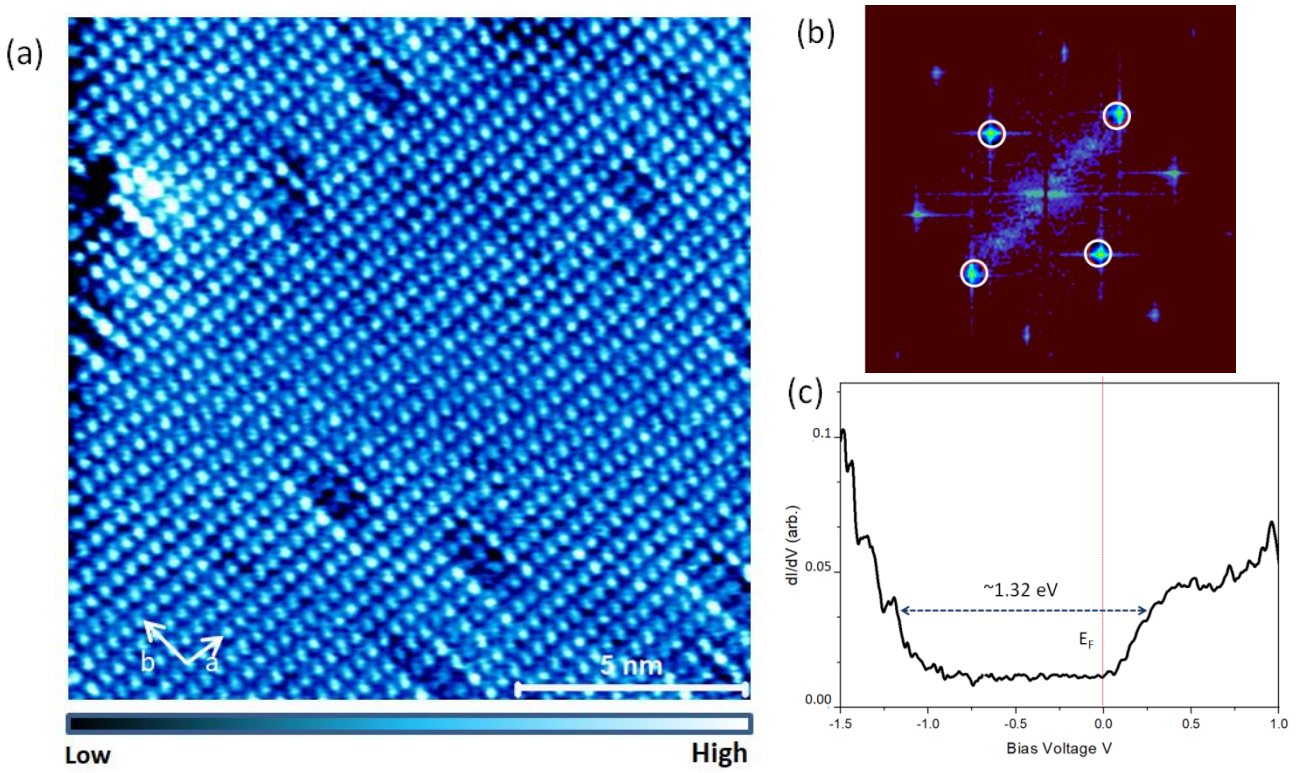


Figure 6.1: STM of CrSBr (a) STM topographic image (15x15 nm, V = -0.5V, $I_t$ = 50 pA) of CrSBr surface. (b) FFT of the Image of figure (a), white circles show the Bragg Peaks. (c) dI/dV (V = -1.5 V, 700 pA) spectra taken on the defect free region shown in the image.

All the STM measurements on Bulk CrSBr were taken in LT-UHV STM at 77 K (sample is in antiferromagnetic phase) with Lock-in sensitivity 500 meV. Figure (6.1 a) shows an atomic resolution STM image taken on less defect region. Figure (6.1b) shows FFT of the rectangular lattice of Br atoms which lie on surface of CrSBr. The marked white circle peaks corresponds to the Bragg peaks of the Surface lattice. The Lattice Parameter calculated from the the FFT shows spacing a = 3.6 Å and b= 4.8 Å with angle 90$^o$ between those lattice vectors which matches with result reported other experiment shown in the figure (6.2). Figure (6.1c) Scanning tunneling spectra dI/dV in pristine area of CrSBr , showing band gap of approximately 1.32 eV which is near to previously reported data(29). The Fermi level is very close to the conduction band ($E_C$-$E_F$ < 200meV). The conduction band starts around 0.18eV and valence band around 1.14eV.(29)

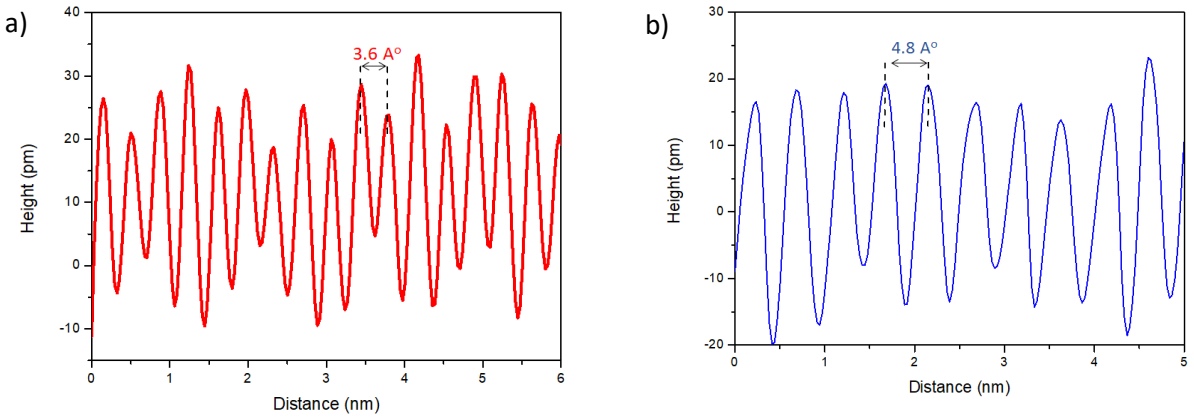


**Figure 6.2**: Height profile along 'a' and 'b' directions are shown with lattice parameter along a = 3.6 Å and b = 4.8 Å.

From the STS data above it is concluded that the CrSBr sample is intrinsic semiconductor nature with band gap of approx. 1.32eV having electrons as majority charge carriers. It has been reported that the bromine vacancies are the main for unintentional electron doping. This offered further idea for investigation of defects.

## 6.1 Probing defects on CrSBr

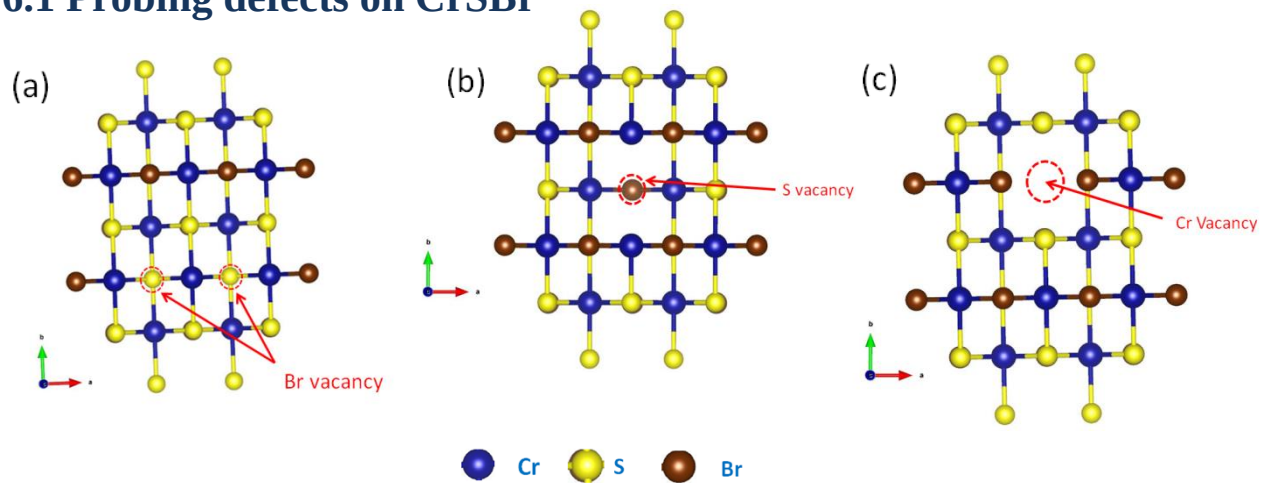


Figure 6.3: Shows Crystal structure of CrSBr with (a) Bromine vacancy (b)Sulphur Vanancy (c) Cr vacancy

The above figure 6.3 shows the crystal structure of CrSBr (top view) showing different elemental vacancies (a) Bromine vacancy (b)Sulphur Vanancy (c) Cr vacancy.

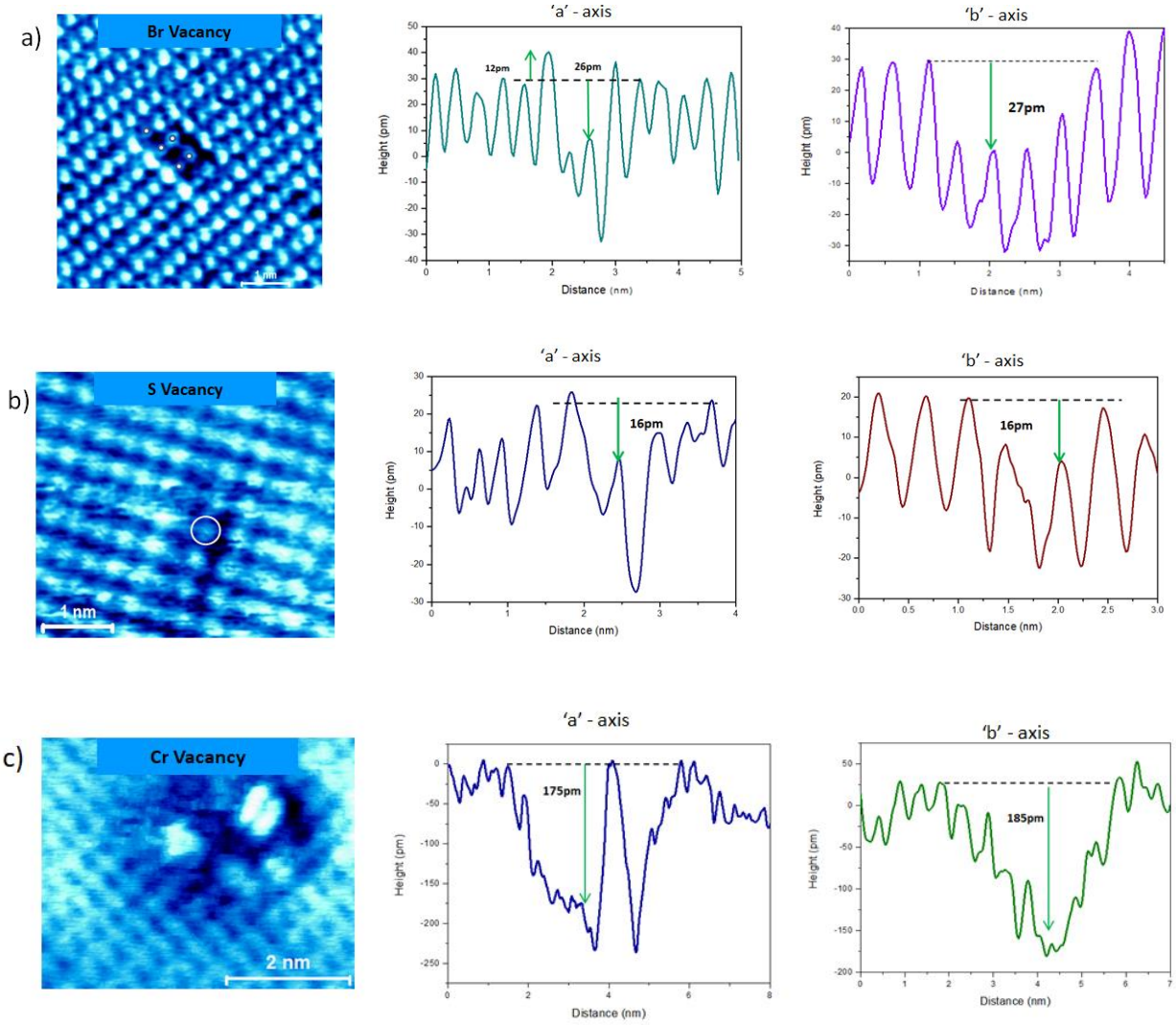


Figure 6.4: STM images of (a)Br vacancy (highlighted by small dots) (b) S Vacancy (highlighted by white circle) (c) Cr Vacancy and corresponding height profile along 'a' – axis and 'b'- axis

STM study of the vacancies was performed to identify and locate various type of defects in the CrSBr sample. CrSBr shows mainly three types of defects as shown above in the figure (6.4). The figure 6.4 (a) shows STM image of Br vacancy which identified by the small with dots . The calculated height difference with surrounding Br atom is 26 pm . The small defect region shows the Sulphur atom situated just below the missing Br atom(35). There is also increase in the electronic contrast brightness around br vacancy along the b-axis and no such signature was seen along the a-axis (shown using increament in height 12pm near the vacancy). This provide evidence

that the b axis is easy axis for electron to flow while in the a-axis there is confinement of electrons showing signature of strong 2D electronic anistropy .(30)

Figure 6.4 (b) shows the STM image of Suphur vacancy (highlighted by white circle) . The calculated height difference shows that there is depression of 16pm and since missing S atom position is situated just below the Br atom ,there is no significant amplitude difference in the oscillation in height of bromine atom b ut Br atom has lower contrast with respect to surrounding bromine atoms.

Figure 6.4 (c) shows a large defect area possibly Cr defects . Cr defect creates high electronic contrast in the region as both Br and S atom attached to Cr atom are also missing. The calculated height difference is around average 180pm (on this defect only) .

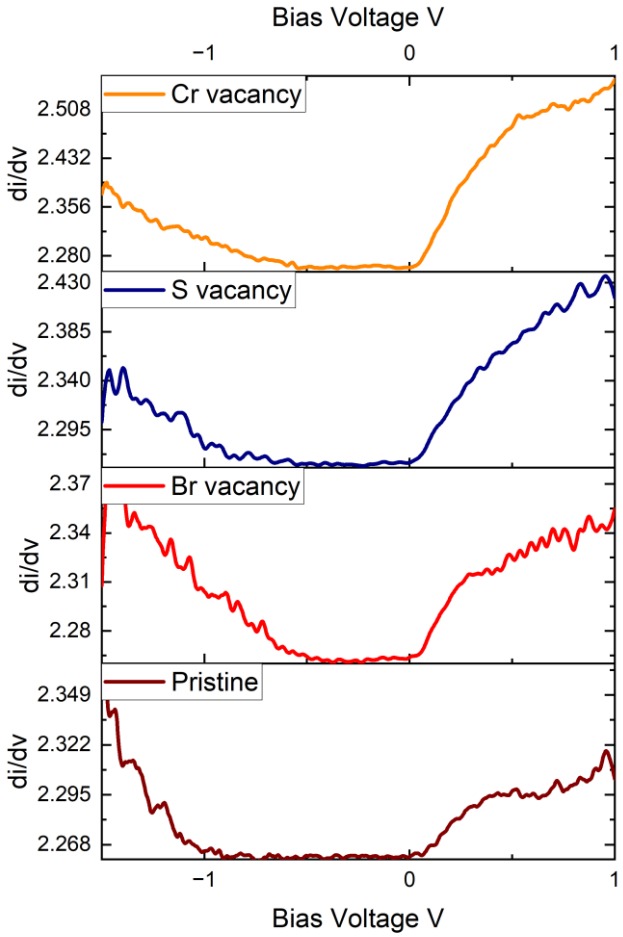


Figure 6.5 shows the point STS spectra on Pristine, Br vacancy, S vacancy, Cr

The figure 6.5 shows the point spectra taken at pristine, Br vacancy, S vacancy and Cr vacancy area. Clearly from the above figure we can conclude that any type of defect will decrease the band gap in the sample. Br and Cr vacancy (approx. band gap 0.67 eV) shows high band gap reduction than that of the S vacancy. (Band gap 1.06eV) shown by shifting of valence band toward fermi level as compared to pristine region point spectra suggesting the defects does facilitate unintentional electron doping in the material. Experiment needs to be performed again at temperature 4K for proper determination of band gap.

## 6.2 Spectroscopic Mapping of Defects

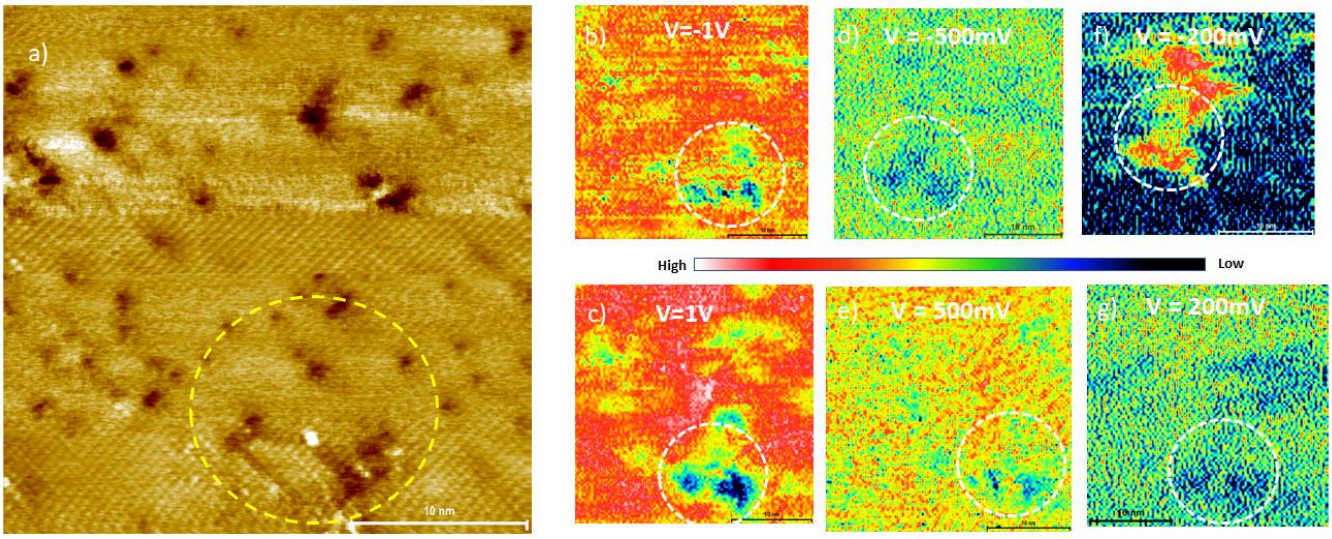


Figure 6.6: Spectroscopic Study of the defect region, (a) shows 30 x 30 nm STM topographic image (V=-1.5, I =300 pA), (b-g) shows the 30 x 30 nm LDOS map (V=1V, I=700pA) at bias -1V, 1V, -500mV ,500mV, -200mV and 200mV

Figure 6.6 shows the LDOS map of defect region as shown above , bias ranging from -1V to 1V . There was no particular difference was noticed in four of the LDOS map of bias of -1V , 1V , -500mV , 500mV. The local density of states is less in the defect region as shown in figure 6.6 (b,c,d,e). But a different signature was noticed at -200mV and 200mV . From figure 6.6 (g) it can be concluded the LDOS of electrons is less defect area but in valence band ( bias at-200mV) , an opposite LDOS contrast is observed. It can be explained as the defect region are forming spacially localised state at energy of -200meV that is not properly evident from STS data given in figure 6.5.

# Chapter 7 Determining Optical band gap of Few Layers $MnPS_3$

In this chapter, we tried determine band gap of the thin flake $MnPS_3$ using optical transmission and absorption spectrometry. All experimental data was obtained in collaboration with Prof. Ashish Arora's lab.

## 7.1 Experimental Setup

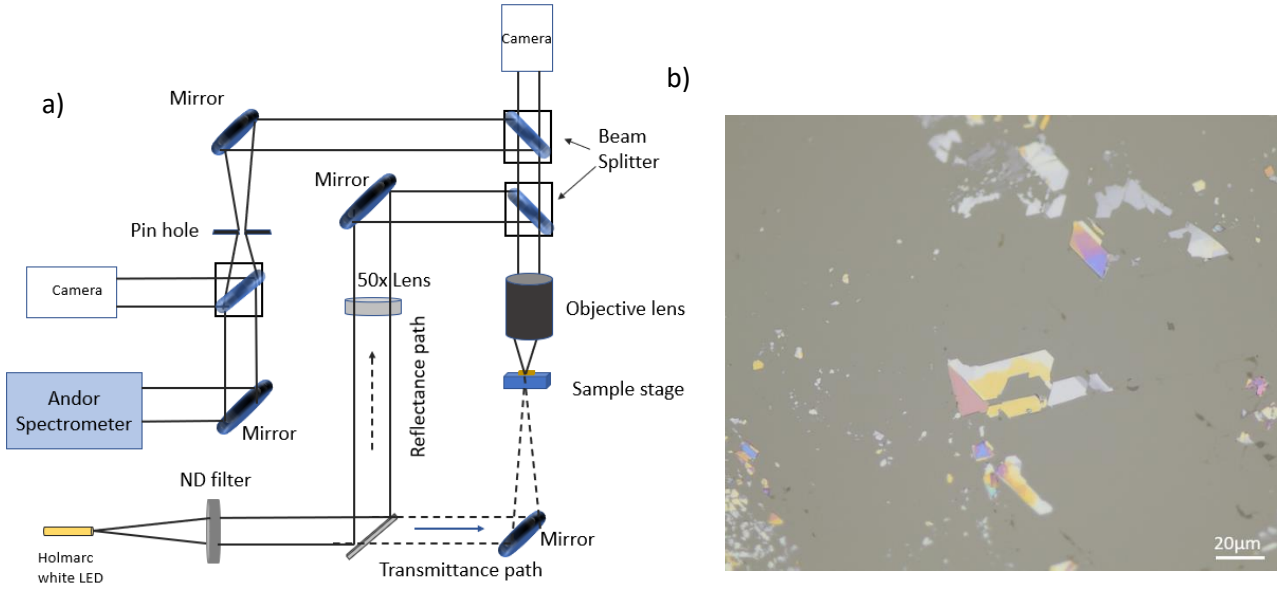


Figure 7.1 Shows the Experimental setup to measure UV-Vis Spectrometry (b) Sample of $MnPS_3$ on sapphire substrate

Figure 7.1 (a) shows the experimental setup to measure the reflectance and absorbance of 2D van der Waal material thin flakes on sapphire substrate (which transparent in nature and gives good response for transmission spectra), Figure (b) 50x magnified sample ($MnPS_3$ on sapphire substrate). All the experiments were conducted in normal incidence mode using halogen white light (unpolarized light). For analyze optical response, a 300mm focal length Andor Kymera Spectrometer with 50 µm slit opening was used. During the experiment exposure time of 0.2s and 100 accumulation steps were kept.

## 7.2 Theory for normal incidence on 2D material free standing sample and on substrate

For free standing sample: A 2D material with a thickness of several nanometer such graphene can be considered as thin film. By using Transfer matrix, we will derive the equation for reflectance, transmittance and absorbance for 2D material at normal incidence.(36)

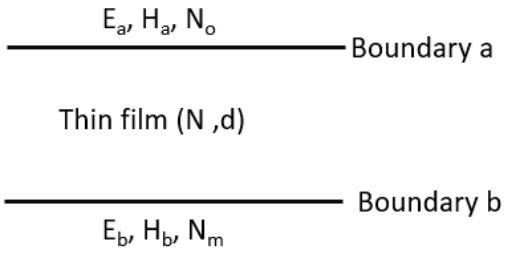


Figure 7.2 Thin film Model for 2D material

Figure 7.2 shows thin film model of 2D material. $E_a$, $H_a$, and $N_o$ represent the electric field, magnetic field, and complex refractive index of air, respectively. Meanwhile, N and d denote the complex refractive index and thickness of the thin film, respectively. $E_b$, $H_b$, and $N_m$ stand for the electric field, magnetic field, and complex refractive index of the substrate.

Applying boundary condition, electric field and the magnetic field vectors between the boundary a and b can be connected in matrix notation as given by equation below:

$$\begin{bmatrix} E_a \\ H_a \end{bmatrix} = \begin{bmatrix} \cos\delta & (i\sin\delta)/y \\ iy\sin\delta & \cos\delta \end{bmatrix} \begin{bmatrix} E_b \\ H_b \end{bmatrix}$$

Where δ is the phase thickness of thin film ($\delta = 2\pi Nd/\lambda$), d is thickness of thin film, λ is the wavelength and *y* (= H/E = NY) is optical admittance of 2D material and Y is optical admittance of free space. The Matrix on RHS part is known as the characteristic matrix.

By normalizing, the electric and magnetic field vector we can write:

$$\begin{bmatrix} E_a/E_b \\ H_a/E_b \end{bmatrix} = \begin{bmatrix} B \\ C \end{bmatrix} = \begin{bmatrix} \cos\delta & (i\sin\delta)/y \\ iy\sin\delta & \cos\delta \end{bmatrix} \begin{bmatrix} 1 \\ y_m \end{bmatrix}$$

Where $y_m$ is optical admittance of substrate.

Considering δ very small because d/λ is less than 0.001 implies cos δ ~ 1 and sin δ ~ δ, the characteristic matrix can be simplified to:

$$\begin{bmatrix} 1 & (i\delta)/y \\ iy\delta & 1 \end{bmatrix}$$

Then as shown in ref(37). Transmittance, reflectance and absorption of 2D material can be calculated by following equations (Fresnel equations):

$$T = \frac{4y_0 \mathrm{Re}(y_s)}{(y_0 B + C)(y_0 B + C)^*}$$

$$R = \left(\frac{y_0 B - C}{y_0 B + C}\right)\left(\frac{y_0 B - C}{y_0 B + C}\right)^*$$

$$A = \frac{4y_0 \mathrm{Re}(BC^* - y_s)}{(y_0 B + C)(y_0 B + C)^*}$$

Setting $N_o = N_m = 1$ the above equation can be written as:

$$T_{TF} = \frac{4}{(2 + 4\pi nkd/\lambda)^2 + 4\pi^2 d^2 (n^2 - k^2 + 1)^2/\lambda^2}$$

$$R_{TF} = \frac{(4\pi nkd/\lambda)^2 + 4\pi^2 d^2 (1 - n^2 + k^2)^2/\lambda^2}{(2 + 4\pi nkd/\lambda)^2 + 4\pi^2 d^2 (n^2 - k^2 + 1)^2/\lambda^2}$$

$$A_{TF} = \frac{4\pi nkd/\lambda + 4\pi^2 d^2 (n^2 - k^2)/\lambda^2}{(1 + 2\pi nkd/\lambda)^2 + \pi^2 d^2 (n^2 - k^2 + 1)/\lambda^2}$$

On substrate sample (normal incidence): Setting $N_o = 1$ and $N_m = n_s$ (refractive index of substrate) the above equation can be written as:

$$A = \frac{4(4\pi nkd/\lambda + 4\pi^2 d^2(n^2 - k^2)n_s/\lambda^2)}{(1 + n_s + 4\pi nkd/\lambda)^2 + (4\pi^2 d^2(n^2 - k^2 + n_s)^2/\lambda^2)}$$

$$T = \frac{4n_s}{(1 + n_s + 4\pi nkd/\lambda)^2 + (4\pi^2 d^2(n^2 - k^2 + n_s)^2/\lambda^2)}$$

$$R = \frac{(1 - n_s - 4\pi nkd/\lambda)^2 + 4\pi^2 d^2(n_s - n^2 + k^2)^2/\lambda^2}{(1 + n_s + 4\pi nkd/\lambda)^2 + (4\pi^2 d^2(n^2 - k^2 + n_s)^2/\lambda^2)}$$

## 7.3 Results and discussion:

Following optical response plots were obtained for different $MnPS_3$ flakes of different thickness and optical band gap was determined.

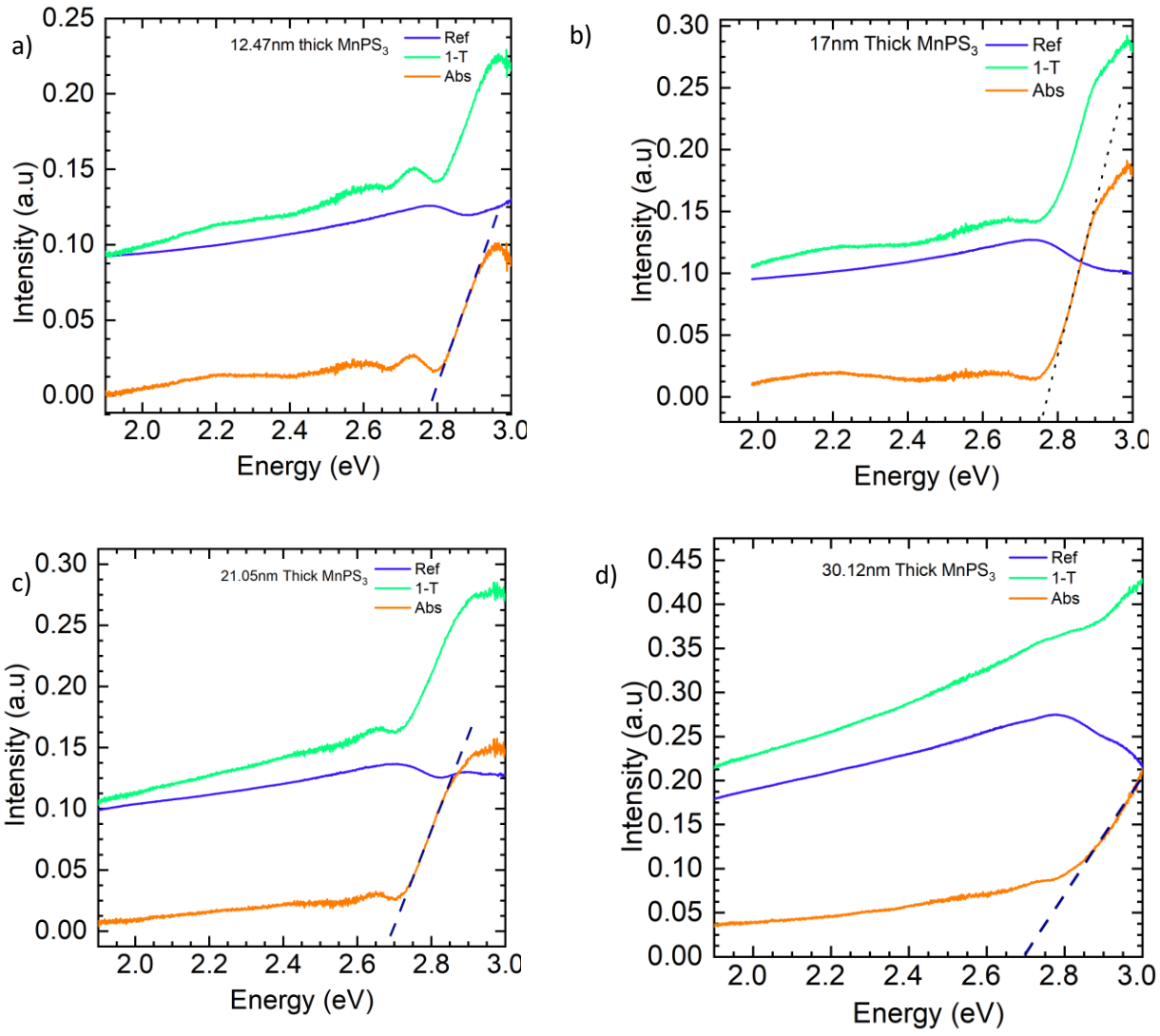


Figure 7.3 Shows the optical response recorded for $MnPS_3$ flake of different thickness.

Clearly evident from the above plots the transmission reaches 100 % at longer wavelengths and there is high absorption at 470 nm showing steep increase in absorbance. The steep increase in absorbance tells us photon energy of wavelength 470nm (E = 2.61 eV) get absorbed by electrons in $MnPS_3$ and make electronic transition valence band to conduction band providing information about material optical band gap.(38–40) The optical band gap found our case:

I. for 12.47nm, $E_g$ = 2.77 eV
II. for 17 nm, $E_g$ = 2.73 eV
III. for 21.05nm, $E_g$ = 2.67 eV
IV. for 30.12nm, $E_g$ = 2.69 eV

# Chapter 8 Conclusion and Future Plans

## Summary of the Work

In this thesis, two van der Waals antiferromagnetic semiconductor material namely $MnPS_3$ ($E_g$ = 2.64eV) and CrSBr ($E_g$ = 1.5 eV) were explored and studied because their different electronic and magnetic properties. $MnPS_3$ and CrSBr were characterized using Optical microscope, atomic force microscope and Raman spectroscopy. $MnPS_3$ optical band gap was determined using UV-vis spectrometry and using STM, defects on CrSBr were probed.

$MnPS_3$ was exfoliated on 3 different substrate ($SiO_2$/Si thickness 0nm ,90nm ,285nm) showing wide range thickness-based color which was quantified using ImageJ software. Thickness of each flake was determined using atomic force microscopy and interference pattern was generated. Raman Spectroscopy was performed on $MnPS_3$ few layers, shows 2 main peaks at $P_1$ = 275.29 $cm^{-1}$ ($E_g$) in-plane vibration method and $P_2$ =383.64 $cm^{-1}$ ($A_g$) out of plane vibration method. No peaks were observed on few layers 1L, 3L, 4L $MnPS_3$ (41,42). We then using UV-VIS spectrometry, optical response of $MnPS_3$ was measured. From the plot we determined the optical band gap of $MnPS_3$ which nearly equal to 2.69 eV(43).

CrSBr was exfoliated on 285nm $SiO_2$/Si substrate and few layers were identified using optical contrast. Atomic force microscopy was performed on those thin crystal flakes for proper determination of thickness. Raman Spectroscopy was performed on those thin flakes of CrSBr, giving 3 intensity peaks at $A^1_g$ = 114 $cm^{-1}$, $A^2_g$ = 244$cm^{-1}$, $A^3_g$ = 344 $cm^{-1}$, all are out of the plane Raman peaks. HR-TEM was performed on CrSBr crystal shows the composition $\mathbf{Cr_{0.67}S_{0.53}Br}$ showing that the there is a higher concentration Cr and S vacancy than Br vacancy in the sample.

STM measurements were performed on Bulk CrSBr at 77K. Best topography image was obtained at V = -0.5V and $I_t$ = 50pA with lattice parameter a = 3.6 Å and b = 4.8 Å with angle of $90^o$ between a and b direction. A detailed study was done on defects on CrSBr. Defects were located and STS was performed on pristine area as well as on defect regions (V = -1.5V, $I_t$ = 700pA). Pristine area shows band gap of approximately 1.32eV which near to reported data of 1.5 eV. The fermi level is found to be near the conduction band which implies the CrSBr is intrinsic electron doped semiconductor. In the defect region both electronic contrast and band gap decreases compared to

pristine region shown by shifting of valence band toward fermi level suggesting the defects does facilitate unintentional electron doping in the material. LDOS mapping was done in defect region shows formation spatially localized state at bias -200meV which not properly evident by STS data taken. This might cause due thermal broadening of the peak at 77K so all the STM and STS experiment need performed at 4K.

## New Advancement made in field of condensed matter

In thesis, STM measurements were performed on CrSBr in its antiferromagnetic phase at 77K. A thorough study was done the defects on CrSBr and results gave us meaningful insight into the defects characters and its role played in making the CrSBr an electron doped material which has been proposed previously(29,30,44). This study will be useful understand electronic correlation in pristine CrSBr region and also in defect regions providing deeper understanding physics of the materials.

Optical Image provides a direct method to determine thin flake $MnPS_3$. Exfoliated sample of $MnPS_3$ showed wide range color variation with respect to thickness. This variation of colour has been quantified showing quasi-periodic oscillatory behavior which is helpful direct identification the thickness of flake. Optical absorbance measurement was performed on thin flake $MnPS_3$ to understand the light matter interaction at room temperature.

## Future Plans

STM measurements need to be performed at 4K. Line spectra along a and b direction need to analyzed. Point Spectra on defects are needed analyzed properly. Need to identify mid gap states in defect region using STS measurements. By forming graphene/hBN/CrSBr heterostructure we tune gate voltage and increase electron concentration in CrSBr which then can be used as sample to be study under STM to understand the effect gating in local region around defects. Temperature dependent -transport experiment on CrSBr need to be performed to understand the electronic anisotropy of the material. Band gap determination using transport measurements still has not been conducted yet which need to be performed.

Few layers $MnPS_3$ refractive index yet to be obtained from optical response data at room temperature and at low temperature under $T_N$ = 78K. By analyzing the optical absorbance at room temperature and under low temperature for thin flakes

# Bibliography


1. Paras, Yadav K, Kumar P, Teja DR, Chakraborty S, Chakraborty M, et al. A Review on Low-Dimensional Nanomaterials: Nanofabrication, Characterization and Applications. Vol. 13, Nanomaterials. MDPI; 2023.

2. Wang QH, Kalantar-Zadeh K, Kis A, Coleman JN, Strano MS. Electronics and optoelectronics of two-dimensional transition metal dichalcogenides. Nat Nanotechnol [Internet]. 2012 [cited 2024 Mar 19];7(11):699–712. Available from: https://pubmed.ncbi.nlm.nih.gov/23132225/

3. Kaxiras E, Joannopoulos JD. Quantum Theory of Materials. Quantum Theory of Materials. Cambridge University Press; 2019.

4. OXFORD MASTER SERIES IN CONDENSED MATTER PHYSICS.

5. Liu Q, Xing J, Jiang Z, Jiang X, Wang Y, Zhao J. 2D tetragonal transition-metal phosphides: An ideal platform to screen metal shrouded crystals for multifunctional applications. Nanoscale. 2020 Mar 28;12(12):6776–84.

6. Mermin ND, Wagner H. Absence of Ferromagnetism or Antiferromagnetism in One- or Two-Dimensional Isotropic Heisenberg Models. Phys Rev Lett [Internet]. 1966 Nov 28 [cited 2024 Mar 27];17(22):1133. Available from: https://journals.aps.org/prl/abstract/10.1103/PhysRevLett.17.1133

7. Rahman S, Torres JF, Khan AR, Lu Y. Recent Developments in van der Waals Antiferromagnetic 2D Materials: Synthesis, Characterization, and Device Implementation. ACS Nano [Internet]. 2021 Nov 23 [cited 2023 Feb 13];15(11):17175–213. Available from: https://pubs.acs.org/doi/full/10.1021/acsnano.1c06864

8. Ningrum VP, Liu B, Wang W, Yin Y, Cao Y, Zha C, et al. Recent Advances in Two-Dimensional Magnets: Physics and Devices towards Spintronic Applications. Research. 2020 Jan 19;2020:1–19.

9. Yu S, Tang J, Wang Y, Xu F, Li X, Wang X. Recent advances in two-dimensional ferromagnetism: strain-, doping-, structural- and electric field-engineering toward spintronic applications. http://www.tandfonline.com/action/journalInformation?show=aimsScope&journalCode=tsta20#VmBmuzZFCUk [Internet]. 2022 [cited 2023 Jan 27];23(1):140–60. Available from: https://www.tandfonline.com/doi/abs/10.1080/14686996.2022.2030652

10. Burch KS, Mandrus D, Park JG. Magnetism in two-dimensional van der Waals materials. Nature 2018 563:7729 [Internet]. 2018 Oct 31 [cited 2021 Dec 28];563(7729):47–52. Available from: https://www.nature.com/articles/s41586-018-0631-z

11. Von Klitzing K. The quantized Hall effect. Rev Mod Phys [Internet]. 1986 Jul 1 [cited 2024 Mar 27];58(3):519. Available from: https://journals.aps.org/rmp/abstract/10.1103/RevModPhys.58.519

12. Li Y, Yang B, Xu S, Huang B, Duan W. Emergent Phenomena in Magnetic Two-Dimensional Materials and van der Waals Heterostructures. ACS Appl Electron Mater [Internet]. 2022 Jul 26 [cited 2024 Mar 19];4(7):3278–302. Available from: https://pubs.acs.org/doi/full/10.1021/acsaelm.2c00419

13. Taylor BE, Steger J, Wold A. Preparation and properties of some transition metal phosphorus trisulfide compounds. J Solid State Chem. 1973 Aug 1;7(4):461–7.

14. Du KZ, Wang XZ, Liu Y, Hu P, Utama MIB, Gan CK, et al. Weak Van der Waals Stacking, Wide-Range Band Gap, and Raman Study on Ultrathin Layers of Metal Phosphorus Trichalcogenides. ACS Nano [Internet]. 2016 Feb 23 [cited 2024 Mar 27];10(2):1738–43. Available from: https://pubmed.ncbi.nlm.nih.gov/26607168/

15. Wildes AR, Rønnow HM, Roessli B, Harris MJ, Godfrey KW. Anisotropy and the critical behaviour of the quasi-2D antiferromagnet, MnPS3. J Magn Magn Mater. 2007 Mar 1;310(2):1221–3.

16. Wildes AR, Rønnow HM, Roessli B, Harris MJ, Godfrey KW. Static and dynamic critical properties of the quasi-two-dimensional antiferromagnet MnPS3. Phys Rev B Condens Matter Mater Phys [Internet]. 2006 Sep 20 [cited 2021 Dec 24];74(9):094422. Available from: https://journals.aps.org/prb/abstract/10.1103/PhysRevB.74.094422

17. Goossens DJ. Dipolar anisotropy in quasi-2D honeycomb antiferromagnet MnPS3. The European Physical Journal B 2010 78:3 [Internet]. 2010 Nov 12 [cited 2021 Dec 27];78(3):305–9. Available from: https://link.springer.com/article/10.1140/epjb/e2010-10569-x

18. Pich C, Schwabl F. Magnetic order of two-dimensional isotropic dipolar antiferromagnets. J Magn Magn Mater. 1995 Feb 1;140–144(PART 3):1709–10.

19. Long G, Henck H, Gibertini M, Dumcenco D, Wang Z, Taniguchi T, et al. Persistence of Magnetism in Atomically Thin MnPS3 Crystals. Nano Lett [Internet]. 2020 Apr 8 [cited 2023 Mar 9];20(4):2452–9. Available from: https://pubs.acs.org/doi/full/10.1021/acs.nanolett.9b05165

20. Kim K, Lim SY, Kim J, Lee JU, Lee S, Kim P, et al. Antiferromagnetic ordering in van der Waals 2D magnetic material MnPS3 probed by Raman spectroscopy. 2d Mater [Internet]. 2019 Jul 10 [cited 2021 Dec 30];6(4):041001. Available from: https://iopscience.iop.org/article/10.1088/2053-1583/ab27d5

21. Zhou Y, He K, Hu H, Ouyang G, Zhu C, Wang W, et al. Strong Neel ordering and luminescence correlation in a two-dimensional antiferromagnet.

22. Frindt RF, Yang D, Westreich P. Exfoliated single molecular layers of Mn0.8PS3 and Cd0.8PS3. J Mater Res. 2005 May;20(5):1107–12.

23. Jin Y, Yan M, Dedkov Y, Voloshina E. Realization of the electric-field driven “one-material”-based magnetic tunnel junction using van der Waals antiferromagnetic MnPX 3 (X: S, Se). J Mater Chem

C Mater [Internet]. 2022 Mar 10 [cited 2023 Feb 14];10(10):3812–8. Available from: https://pubs.rsc.org/en/content/articlehtml/2022/tc/d1tc05922j

24. Luong DH, Phan TL, Ghimire G, Duong DL, Lee YH. Revealing antiferromagnetic transition of van der Waals MnPS3 via vertical tunneling electrical resistance measurement. APL Mater [Internet]. 2019 Aug 1 [cited 2023 Feb 14];7(8):081102. Available from: https://aip.scitation.org/doi/abs/10.1063/1.5112130

25. Goossens DJ, Studer AJ, Kennedy SJ, Hicks TJ. The impact of magnetic dilution on magnetic order in MnPS3. Journal of Physics: Condensed Matter [Internet]. 2000 May 8 [cited 2021 Dec 23];12(18):4233. Available from: https://iopscience.iop.org/article/10.1088/0953-8984/12/18/308

26. Chandrasekharan N, Vasudevan S. Dilution of a layered antiferromagnet: Magnetism in <span class. Phys Rev B [Internet]. 1996 Dec 1 [cited 2021 Dec 24];54(21):14903. Available from: https://journals.aps.org/prb/abstract/10.1103/PhysRevB.54.14903

27. Katscher H, Hahn H. Über Chalkogenidhalogenide des dreiwertigen Chroms. Naturwissenschaften [Internet]. 1966 Jan [cited 2024 Mar 27];53(14):361. Available from: https://link.springer.com/article/10.1007/BF00621875

28. López-Paz SA, Guguchia Z, Pomjakushin VY, Witteveen C, Cervellino A, Luetkens H, et al. Dynamic magnetic crossover at the origin of the hidden-order in van der Waals antiferromagnet CrSBr. Nat Commun. 2022 Dec 1;13(1).

29. Telford EJ, Dismukes AH, Lee K, Cheng M, Wieteska A, Bartholomew AK, et al. Layered Antiferromagnetism Induces Large Negative Magnetoresistance in the van der Waals Semiconductor CrSBr. Advanced Materials. 2020 Sep 1;32(37).

30. Wu F, Gutiérrez-Lezama I, López-Paz SA, Gibertini M, Watanabe K, Taniguchi T, et al. Quasi-1D Electronic Transport in a 2D Magnetic Semiconductor. Advanced Materials. 2022 Apr 1;34(16).

31. Klein J, Pingault B, Florian M, Heißenbüttel MC, Steinhoff A, Song Z, et al. The Bulk van der Waals Layered Magnet CrSBr is a Quasi-1D Material. ACS Nano. 2023 Mar 28;17(6):5316–28.

32. Voigtländer B. Scanning Probe Microscopy. 2015 [cited 2024 Mar 27]; Available from: https://link.springer.com/10.1007/978-3-662-45240-0

33. Torres K, Kuc A, Maschio L, Pham T, Reidy K, Dekanovsky L, et al. Probing Defects and Spin-Phonon Coupling in CrSBr via Resonant Raman Scattering. Adv Funct Mater [Internet]. 2023 Mar 1 [cited 2024 Mar 19];33(12):2211366. Available from: https://onlinelibrary.wiley.com/doi/full/10.1002/adfm.202211366

34. Pei F, Yu J, Zhou J, Wang S, Liu D, Yuan Y, et al. Surface-Sensitive Detection of Magnetic Phase Transition in Van Der Waals Magnet CrSBr. Adv Funct Mater. 2023;

35. Vancsó P, Magda GZ, Peto J, Noh JY, Kim YS, Hwang C, et al. The intrinsic defect structure of exfoliated MoS2 single layers revealed by Scanning Tunneling Microscopy. Sci Rep. 2016 Jul 22;6.

36. Wang X, Chen B. Origin of Fresnel problem of two dimensional materials. Sci Rep. 2019 Dec 1;9(1).

37. Hecht Eugene. Optics. Addison-Wesley; 2002. 698 p.

38. Harms NC, Kim HS, Clune AJ, Smith KA, O'Neal KR, Haglund A V., et al. Piezochromism in the magnetic chalcogenide MnPS3. NPJ Quantum Mater. 2020 Dec 1;5(1).

39. Frindt RF, Yang D, Westreich P. Exfoliated single molecular layers of Mn0.8PS3 and Cd0.8PS3. J Mater Res. 2005 May;20(5):1107–12.

40. Ummah AM, Peng YH, Ho CH. Structure, property and magneto-optical interaction of wide-band-gap layered magnetism near the Néel temperature with antiferromagnetic to paramagnetic transition. FlatChem. 2023 Sep 1;41.

41. Ummah AM, Peng YH, Ho CH. Structure, property and magneto-optical interaction of wide-band-gap layered magnetism near the Néel temperature with antiferromagnetic to paramagnetic transition. FlatChem. 2023 Sep 1;41.

42. Zhou Y, He K, Hu H, Ouyang G, Zhu C, Wang W, et al. Strong Neel ordering and luminescence correlation in a two-dimensional antiferromagnet.

43. Harms NC, Kim HS, Clune AJ, Smith KA, O'Neal KR, Haglund A V., et al. Piezochromism in the magnetic chalcogenide MnPS3. NPJ Quantum Mater. 2020 Dec 1;5(1).

44. Moro F, Ke S, del Águila AG, Söll A, Sofer Z, Wu Q, et al. Revealing 2D Magnetism in a Bulk CrSBr Single Crystal by Electron Spin Resonance. Adv Funct Mater. 2022 Nov 3;32(45).